ISBN No:978-93-5391-753-1

Proceedings of the National Seminar on

NEW HORIZONS IN THEORETICAL AND EXPERIMENTAL PHYSICS

Organized by

Department of Physics

S.A.R.B.T.M Govt. College, Koyilandy

Sponsored by

Directorate of Collegiate Education, Thiruvananthapuram

November 2019

Editor: Nithu Ashok

Proceedings of the National Seminar on

NEW HORIZONS IN THEORETICAL AND EXPERIMENTAL PHYSICS

ISBN NUMBER: 978-93-5391-753-1

Chief Editor
Dr. Nithu Ashok

Organized by

Department of Physics
S.A.R.B.T.M Govt. College, Koyilandy

Sponsored by

Directorate of Collegiate Education,
Thiruvananthapuram

Proceedings of the National Seminar on
NEW HORIZONS IN THEORETICAL AND EXPERIMENTAL PHYSICS

Editors

Chief Editor
Dr. Nithu Ashok

Editorial Board
Dr. Rajita Ramanarayanan
Dr. Simji P
Dr. Honey M

First Edition : November 2019

ISBN NUMBER: 978-93-5391-753-1

FOREWORD

As a progressive society we need to keep ourselves updated with the latest developments in the field of science and technology. The two National Seminar on New Horizons in theoretical and experimental Physics provides a scientific platform for the students and young researchers to discuss their work and interact with other eminent personalities. The aim of the book is to give the researchers a platform to publish their work and inspire student community towards the need of research. Our seminar covers various areas like nuclear physics, non linear dynamics, nanotechnology, astrophysics etc.

We are grateful to our Principal, Prof. Anwar Sadath M for giving us constant support and encouragement in organizing the two day national seminar. We are also thankful to Directorate of Collegiate Education, Thiruvananthapuram for providing financial support for the conduct of national seminar. All the teachers and non-teaching staff of the department who helped in the smooth conduct of the seminar is duly acknowledged.

Dr. Nithu Ashok
Chief Editor

Dedicated to
ALMIGHTY

CONTENTS

Exotic decay possibilities of various proton halo nuclei in the Super heavy region

K. P. Anjali[1], K. Prathapan[1] and R. K. Biju[2]
[1]Department of Physics, Govt. Brennan College, Thalassery,-670106
[2]Department of Physics, Pazhassi Raja NSS College, Mattannur, Kerala - 670702

Abstract

Based on the Coulomb and Proximity Potential Model (CPPM), we have studied the decay probabilities of various proton halo nuclei ^{9}C, ^{20}Mg and ^{28,29}S from some of the elements in the superheavy region by computing the decay half-lives and other characteristics. From the plot connecting half-life against neutron number of daughter nuclei, we can observe certain peaks and dips, which indicate the shell closure effect of parent and daughter nuclei respectively. Neutron shell closure of daughter nuclei at N$\sim$ 142 and the parent shell closure at N$\sim$ 152 are visible from these plots. We have also studied the Geiger-Nuttall plots for various proton halo nuclei emitting from the superheavy parent isotopes with Z=119. From the plots, we can find that inclusion of proximity potential does not produce significant deviation from the linear nature of the Geiger-Nuttall plots.

Introduction

The half-life of any nuclear decay provides a powerful tool for determining the stability of various elements in the superheavy region. The region that lies above Rutherfordium ($Z = 104$) is termed as a superheavy region[1]. The search for superheavy nuclei has shown remarkable growth over the past few years. The researchers were successful in synthesizing elements up to $Z = 118$ by cold fusion reaction[2] and hot fusion reaction[3]. The elements with $Z > 118$ are still unknown, but the attempt to synthesize $Z = 120$[4] is running in GSI in Darmstadt. We have selected $Z = 115 - 120$ for our study, among these, elements with $Z = 114$ to 118 have been successfully synthesized at JINR- FLNR, Dubna, in collaboration with LLNL[5, 6]. Superheavy elements help us introduce the concept of magic numbers and the island of stability, which explains the additional stability of specific elements in this region. Previously, several studies have been conducted to predict the likelihood of various nuclear decays from superheavy parent[7, 8]. In the present work, we have studied the decay possibilities of various proton

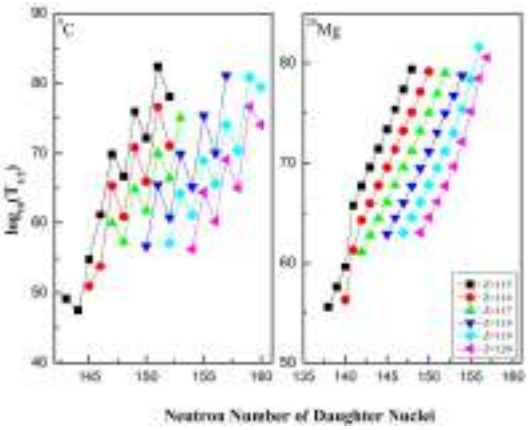

Figure 1: Plot of $log_{10}T_{1/2}$ versus neutron number of the daughter nuclei from Z=115-120 for the decay of ^{9}C and ^{20}Mg.

halo nuclei in the superheavy region. Proton halo nuclei are the proton-rich exotic nuclei located near the proton drip line[9]. Their proton density distribution shows a much-extended tail and it has weak binding energy and large spatial dimension of the outermost nuclei. The study of proton halo nuclei is one of the major challenges in experimental and theoretical nuclear physics. There have been many experimental and theoretical studies to understand the structure of proton halo nuclei[10, 11]. Due to the very low half-life, the structure of the halo nuclei is mainly studied by radioactive nuclear beams. There are different models available to calculate the half-lives of the elements. CPPM is one of the most established models to calculate the lifetime of the elements[12], and that we have used in the present contribution, to study the existence of proton halo nuclei.

The Model

The total interacting potential barrier for the parent nuclei showing exotic decay is given by

$$V = \frac{Z_1 Z_2 e^2}{r} + V_p\left(z\right) + \frac{\hbar^2 l\left(l+1\right)}{2\mu r^2},\ z > 0 \tag{1}$$

$V_p(z)$ is the proximity potential which is given by Blocki et al.[13]

$$V_p(z) = 4\pi\gamma b[\frac{C_1 C_2}{C_1 + C_2}]\Phi(\frac{z}{b}) \tag{2}$$

The surface tension coefficient γ given by

$$\gamma = 0.9517[1 - 1.7826(N-Z)^2/A^2]MeV/fm^2 \tag{3}$$

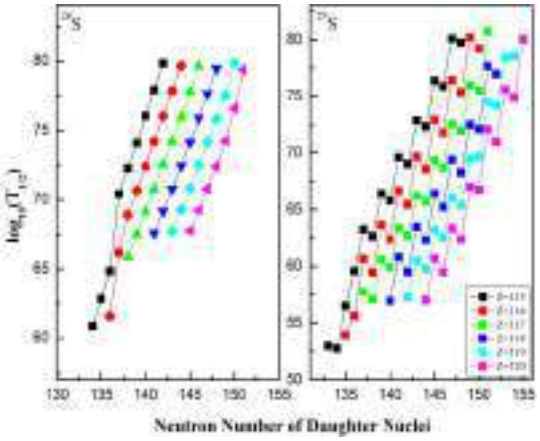

Figure 2: Plot of $log_{10}T_{1/2}$ versus neutron number of the daughter nuclei from Z=115-120 for the decay of ^{28,29}S.

Φ represents the universal proximity potential given as[14]

$$\Phi(\varepsilon) = -4.41e^{-\varepsilon/0.7176}, for\ \varepsilon > 1.9475 \tag{4}$$

$$\Phi(\varepsilon) = -1.7817 + 0.9270\varepsilon + 0.0169\varepsilon^2 - 0.05148\varepsilon^3,\ for\ 0 \leq \varepsilon \leq 1.9475 \tag{5}$$

Using the one dimensional WKB approximation, barrier penetrability P is given by

$$P = \exp\left\{-\frac{2}{\hbar}\int_a^b \sqrt{2\mu(V-Q)}dz\right\} \tag{6}$$

The half-life of this decay process is given by

$$T_{1/2} = \frac{ln\ 2}{\lambda} = \frac{ln\ 2}{\nu P} \tag{7}$$

Results and Discussion

In the present work, we have computed the decay half-lives and other characteristics of proton halo nuclei ^{9}C, ^{20}Mg and ^{28,29}S by using the Coulomb and Proximity Potential Model as the interacting barrier. Figures 1 and 2 give the plots of decay half-lives of different superheavy parents against the neutron number of the daughter nuclei. We have selected superheavy parent isotopes $^{261\text{-}278}$115, $^{264\text{-}279}$116, $^{267\text{-}284}$117, $^{271\text{-}283}$ 118, $^{274\text{-}288}$119 and $^{277\text{-}285}$120 for the emission of two proton halo nuclei ^{9}C, ^{20}Mg, ^{28,29}S. From these figures, we can find some peaks and dips that indicate the shell closure of parent and daughter nuclei respectively. The ^{9}C emission from ^{265}115, ^{266}116 in figure 1 shows considerable peaks that represent the parent shell

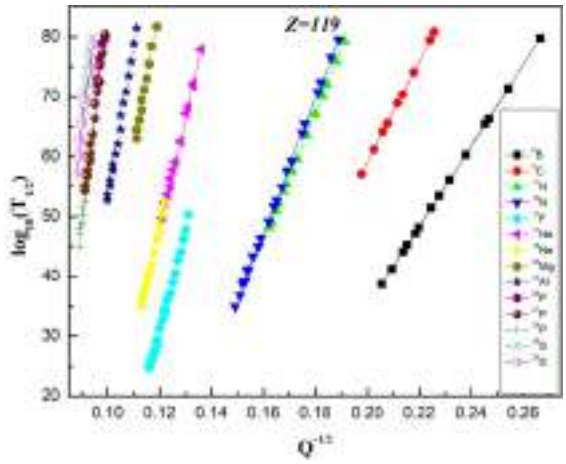

Figure 3: Geiger-Nuttall plot of $log_{10}T_{1/2}$ values versus $Q^{-1/2}$ for various proton halos from superheavy nuclei with Z=119.

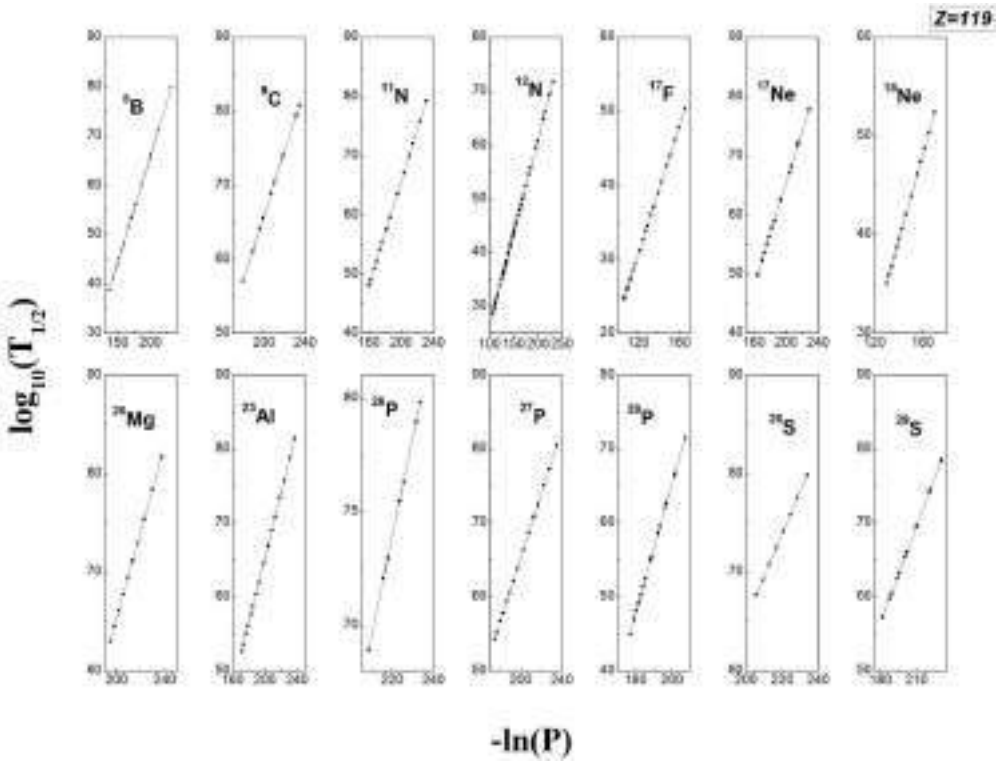

Figure 4: The universal curve for calculated negative logarithm of penetrability versus logarithmic half-lives for various proton halos from the superheavy nuclei with Z=119.

closure at Np= 150. A dip can be observed at Nd= 144 representing the neutron shell closure of daughter nuclei. It is also obvious from figure 2 that shell closure of parent occurs at N=150 and shell closure of daughter occurs at N$\sim$ 134 in the case of ^{29}S. We would like to mention that our observations are consistent with the earlier findings in which neutron shell closure is predicted at N=152[15, 16].

In the next part of our work, Geiger Nuttall curves are drawn for all the observed or predicted cases of proton halo nuclei from the parent with Z=119. Figure 3 shows the graph of $log_{10}T_{1/2}$ vs. $Q^{-1/2}$ and the plots are found to be linear with different slopes and intercepts. Figure 4 shows Universal curve between $-ln\ P$ and $log_{10}T_{1/2}$ of all the proton halo decays and the plots are found to be linear with the same slope and intercept. The linearity in these figures says that the inclusion of proximity potential does not change the linearity of the plot and Geiger Nuttall law is valid for the proton halo decay also.

Conclusion

- Half-life and other characteristics for the emission of two proton halo nuclei ^{9}C, ^{20}Mg, ^{28,29}S from different superheavy parent nuclei are calculated using CPPM.
- Based on the observations, we have identified that N$\sim$ 152 is a parent neutron shell closure, hence the extra stability is attained at this neutron number.
- The GN plot and universal curve say that the linearity does not change with the inclusion of proximity potential, so GN law is valid for the proton halo decay also.

References

[1] U. Mosel and W. Greiner, *Z. Phys. A*, 222, 261 (1969)

[2] Y. Oganessian, *J. Phys. G: Nucl. Part. Phys.*, 34, R165 (2007)

[3] S. Hofmann, *Physics*, 3, 31 (2010)

[4] Y. T. Oganessian et al. *Phys. Rev. C*, 79, 024603 (2009)

[5] Y. Oganessian et al. *Phys. Rev. Lett*, 104, 142502 (2010)

[6] D. Ghiorso et al. *Nucl. Phys. A*, 583, 861 (1995)

[7] K. P.Santhosh and B. Priyanka, *Nucl. Part. Correla. Cluster Phys.*, 383 (World Scientific, 2017)

[8] G. Naveya, S. Santhosh Kumar, S. I. A. Philominraj and A. Stephen, *Int. J. Mod. Phys. E*, 28, 1950051 (2019)

[9] G. Saxena and D. Singh, *J. Exp. Theor. Phys.*, 116, 567 (2013)

[10] K.P. Santhosh and I. Sukumaran, *Pramana J. Phys.*, 92, 1 (2019)

[11] G. Saxena et al. *Phys. Lett. B*, 775, 126 (2017)

[12] K.P. Santhosh, R.K. Biju and A. Joseph, *J Phys G: Nucl. Part. Phys.*, 35, 085102 (2008)

[13] J. Blocki et al. *Ann. Phys.*, 105, 427 (1977)

[14] J. Blocki and W.J. Sweatecki, *Ann. Phys.*, 132, 53 (1981)

[15] M. Ismail, I. A. M. Abdul-Magead and Samar Gamal, *IOSR J. Appl. Phys.*, 9, 64 (2017)

[16] M. Ismail, A. Y. Ellithi, M. M. Botros and A. Adel, *Phys. Rev. C*, 81, 024602 (2010)

Spatial Solitons in one and two Dimensional Systems

Dr. Aysha Muhsina K [1], Haris U[2]
[1]Department of Physics, N.M.S.M Govt College, Kalpetta
[2]Dept. of Computer Science, K.A.H.M Unity women's college, Manjeri

Abstract

This work analyzes the dynamics of spatial solitons in one dimensional and two dimensional media. The study has been done by variational analysis and numerically by finite difference method. The presence of dffraction in the medium results in the beam broadening and nonlinearity results in the beam steepening. When there is a balance between diffraction and nonlinearity, the beam propagates in the form of stable waves called solitons. In a homogenous (1+1)D medium, the balancing between diffrraction and nonlinearity is enough to produce soliton beam propagation. But a two dimensional system is highly sensitive to nonlinearity. In such systems the diffraction alone may not be sufficient to balance the nonlinearity to form solitons. If the medium is inhomogeneous, the dissipation along with the diffraction balance the nonlinear induced steepening and results in soliton propagation.

Introduction

Solitons are special kinds of wave packets which propagate undistorted over long distances, which are caused by the cancelation of nonlinear and dispersive effects in the medium. They were first observed by a Scottish naval architect named John Scott Russel in 1834. He was conducting experiments near Edinburgh to determine the most efficient design for canal boats. During his experiments he observed that a heap of water in a canal propagated undistorted over several kilometers. He called them as the great wave of translation, which represents the first scientific account of solitons in history. These water wave formed in the narrow channel exhibited some strange properties. They were highly stable, neither attenuated out nor steepened like normal waves. Even after the collision with other similar waves, they would not merge with each other waves. A small wave traveling faster would overtake a large one traveling slower. Due to this particle like properties, these waves were named as soitons [1]. Solitons have been extensively studied in many branches of physics such as optics, plasmas, condensed matter physics,

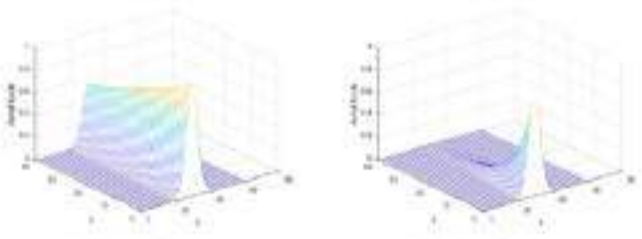

(c) $\beta = 1, d = 0.001$ (d) $\beta = 1, d = 0.009$

Figure 1. Beam propagation in a (1+1)D nonlinear medium. In fig. (a), the diffraction coefficient is low. In fig (b), the diffraction coefficient is higher and beam spreading is also higher

fluid mechanics, particle physics and even astrophysics [2],[3]. They have important applications in optics, especially in optical communication systems for achieving distortion less data transmission, optical switching etc. Soliton based optical communication systems can be used over distances of several thousands of kilometers with huge information carrying capacity. The discovery of solitons in optical fibre was done by Zhakarov and Sabat in 1971 [4]-[6]. Optical Solitons are the self-trapped wave-packets that propagate in a nonlinear medium with diffraction. A wave packet has a natural tendency to spread as it propagates in a medium, either due to chromatic dispersion or due to spatial diffraction. In the propagation of low light intensity pulses, the properties of materials remain independent of the intensity of the pulse. When the incident intensity is sufficiently high, the refractive index of the fiber has an intensity dependent component because of the nonlinear Kerr effect. The intensity dependent refractive index leads to a large number of nonlinear effects like self-phase modulation (SPM) and cross-phase modulation (XPM) [7],[8]. The effect of SPM is to steepen the wave. When the broadening due to dispersion/diffraction is eliminated through a SPM induced steepening, a stable self localized wave packet propagates. Such a self-trapped wave-packet is known as an optical soliton.

Optical solitons can be either temporal or spatial depending upon whether they are confined in time or space during propagation. In spatial optical solitons the beam steepening is balanced by broadening due to diffraction. The dynamics of spatial optical soliton is governed by Nonlinear Schrodinger Equation (NLSE) [9], which contains the terms corresponding to diffraction caused by the finite size of the wave and self focusing nonlinearity of the medium. This wok analyzes the dynamics of spatial solitons in (1+1)D and (2+1)D homogeneous media. The paper is divided into four sections. Section (2) gives the mathematical modeling of the optical beam propagation through (1+1)D and (2+1)D nonlinear media. In section (3) and (4), the beam dynamics has been analyzed in one and two dimensional nonlinear

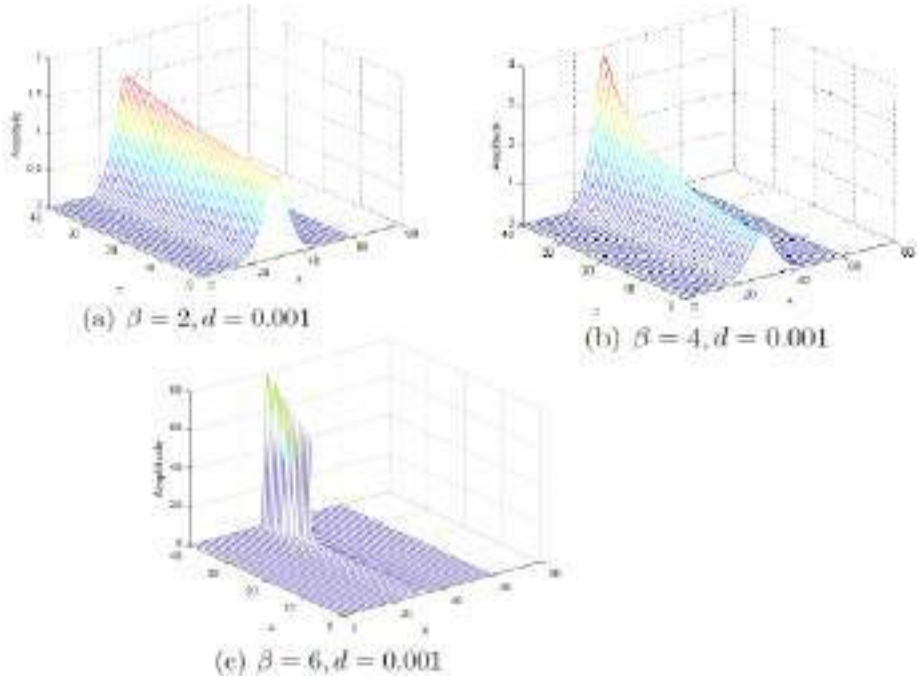

(a) $\beta = 2, d = 0.001$

(b) $\beta = 4, d = 0.001$

(c) $\beta = 6, d = 0.001$

media using numerical studies. The results are concluded in section (5).

2. Mathematical modeling of the spatial solitons in (1+1)D and (2+1)D medium

The optical beam propagation in one dimensional nonlinear medium is governed by Nonlinear Schrodinger Equation (NLSE) of the form [9];

$$i\Psi_z + d\Psi_{xx} + \beta|\Psi|^2\Psi = 0 \tag{1}$$

Where d is the diffraction and β is the co-efficient of nonlinearity. (β = + (-) 1 represents self focusing (self defocusing) nonlinearity of the medium). The optical beam propagation in a two dimensional dissipative medium is given by [12],[13];

$$i\Psi_z + d(\Psi_{xx} + \Psi_{yy}) + \beta|\Psi|^2\Psi = 0 \tag{2}$$

Where the subscripts stand for the partial derivatives are with respect to z, x and y respectively. $\psi\,(x, y, z)$ is the wave function of the wave envelope. Applying the condition for radial symmetry, $x^2+y^2 = r^2$ and $\nabla^2 = \frac{1}{r}\frac{\partial}{\partial \mathrm{r}} + \frac{\partial^2}{\partial r^2}$, equation (2) becomes

$$i\Psi_z + d(\frac{1}{r}\Psi_r + \Psi_{rr}) + \beta|\Psi|^2\Psi = 0 \tag{3}$$

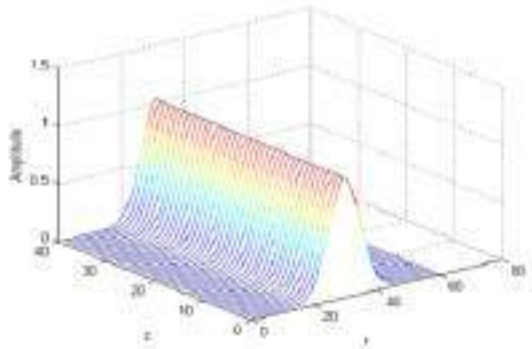

Figure 3. Stable spatial solitons formed in 1D medium. $\beta = 1, d = 0.005$

Numerical Analysis

The partial differential equations (1) and (3) have been studied numerically by using finite difference method [14]. In this method a rectangular grid has been considered for the problem and the grid planes are equally spaced as Δ z and Δ r in propagation and radial dimension respectively; z = s Δ z and r = n Δ r. The intervals are selected such that the condition for stability $\frac{\Delta z}{(\Delta r)^2} \leq 0.5$, is satisfied. Here the partial derivatives are replaced by difference equations as; $\frac{\partial \Psi}{\partial z} = \frac{\Psi_n^{s+1} - \Psi_s^s}{2\Delta z}$ and $\frac{\partial^2 \Psi}{\partial^2 \mathrm{x}} = (\frac{\Psi_{n+1}^{s+1} - 2\Psi_n^{s+1} + \Psi_{n-1}^{s+1}}{\Delta x^2} + \frac{\Psi_{n+1}^{s-} + 2\Psi_n^s + \Psi_{n-1}^s}{\Delta x^2})$ These substitutions in NLSE (1) results in a matrix equation of the form;

$$\begin{bmatrix} A_2 & A_1 & 0 & 0 & 0 & 0 & . \\ A_3 & A_2 & A_1 & 0 & 0 & 0 & . \\ 0 & A_3 & A_2 & A_1 & 0 & 0 & . \\ . & . & . & . & . & . & . \\ . & . & . & . & . & . & . \end{bmatrix} \begin{bmatrix} \Psi_1^{s+1} \\ \Psi_2^{s+1} \\ \Psi_3^{s+1} \\ . \\ . \end{bmatrix} = \begin{bmatrix} B_2 & B_1 & 0 & 0 & 0 & 0 & . \\ B_3 & B_2 & B_1 & 0 & 0 & 0 & . \\ 0 & B_3 & B_2 & B_1 & 0 & 0 & . \\ . & . & . & . & . & . & . \\ . & . & . & . & . & . & . \end{bmatrix} \begin{bmatrix} \Psi_1^s \\ \Psi_2^s \\ \Psi_3^s \\ . \\ . \end{bmatrix}$$

Where A_1, A_2, A_3, B_1, B_2, B_3 are the tri-diagonal matrix elements which are given as;

$$A_1 = A_3 = \frac{2\Delta z d}{\Delta x^2} \tag{4}$$

$$A_2 = i - \frac{4\Delta z d}{\Delta x^2} + 2\Delta z \beta |\Psi_n^{s+1}|^2 \tag{5}$$

$$B_1 = B_3 = -\frac{2\Delta z d}{\Delta x^2} \tag{6}$$

$$B_2 = i + \frac{4\Delta z d}{\Delta x^2} - 2\Delta z \beta |\Psi_n^{s+1}|^2 \tag{7}$$

An initial Guassian wave function was chosen for Ψ and the beam dynamics is studied using the above matix equation.

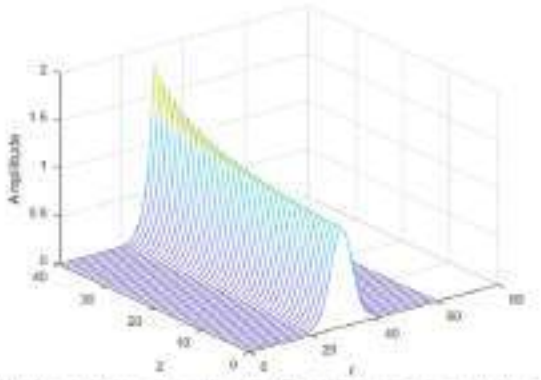

Figure 4. Beam dynamics in 2D medium $\beta = 1, d = 0.005$

Beam Dynamics in (1+1)D medium

The beam propagation is analyzed in (1+1) D medium. The coefficient of nonlinearity is considered as β =1 and the diffraction coefficient d is varied. The beam dynamics is shown in figure (1). The effect of diffraction is to broaden the beam. The beam spreads more as the diffraction coefficient, d increases. Figure (2) shows the propagation when the diffraction coefficient $d = 0.001$. The nonlinearity in the medium results in the beam steepening as shown in figure. As the nonlinearity coefficient increases, beam sharpens more and more and finally it results in the breaking of the beam due to self phase modulation as shown in figure (2.c).

When both the diffraction coefficient and nonlinearity coefficient balances, the beam propagates constantly without any change in their shape or size, as shown in figure(3). This is called Soliton beam propagation. in a homogenous (1+1)D medium, the balancing between diffraction and nonlinearity is enough to produce soliton beam propagation.

Beam Dynamics in (2+1)D medium

The study has been extended to two dimensional nonlinear medium. The coefficients of nonlinearity and diffraction, which results in the soliton formation in one dimensional systems, results in a different type of dynamics in two dimensional medium. Beam propagation in 2D medium is not stable as shown in figure (4), which is plotted for the same parameters of figure (3) (β = 1; d = 0:005). This medium is highly sensitive to the nonlinear changes. A small value of nonlinearity coefficient is enough to result in stable beam propagation. Figure (5.a) shows the solitons formed in a two dimensional for the parameters β = 0:05; d =0.005. Here the nonlinearity coefficient is negligible. A small change in the nonlinearity coefficient results in the

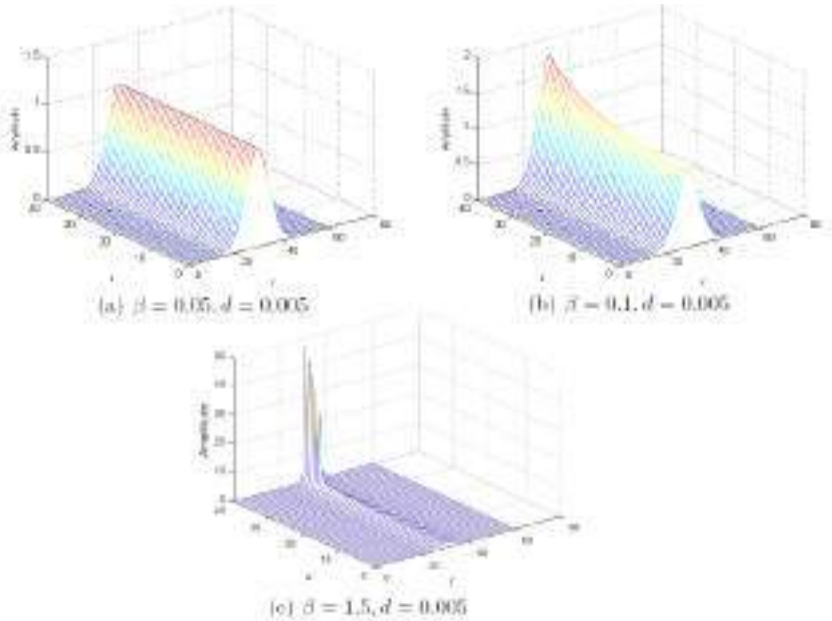

(a) $\beta = 0.05, d = 0.005$ (b) $\beta = 0.1, d = 0.005$

(c) $\beta = 1.5, d = 0.005$

Figure 5. Beam dynamics in 2D nonlinear medium for different values of β. The beam stabilizes as β decreases

steepening of the beam and finally the beam collapses as shown in figure (5.b) and (5.c). In a (2+1)D homogeneous medium, the diffraction induced broadening of the beam alone are not sufficient to balance the nonlinear effects. In such systems the existence of some dissipation mechanisms is essential for the soliton propagation. In an inhomogeneous higher dimensional system, the balancing between nonlinearity and diffraction along with the dissipation effects due to inhomogenity may result in soliton propagation. Such solitons are known as Dissipative Solitons.

Conclusion

This work analyzed the beam dynamics in (1+1)D and (2+1)D nonlinear medium. In a linear medium, the presence of diffraction results in the broadening of the beam. The effect of nonlinearity is to steepen the beam. When both the effects are present, their balancing results in the propagation of stable wave called solitons. In a homogenous one dimensional medium, the balancing between diffraction and nonlinearity is enough to produce soliton beam propagation. But in a (2+1)D medium, the system is highly sensitive to the nonlinear changes. Diffraction alone is not sufficient to balance the nonlinear induced steepening. Any small change in nonlinearity may result in the soliton collapse. If the two dimensional medium is dissipative effects should present in the medium for soliton propagation.

References

[1] N. J. Zabusky and M. D. Kruskal, *Rev. Lett.*, **15**, 240 (1965).

[2] N. N. Akhmediev and A. A. Ankiewicz, *Solitons Nonlinear Pulses and Beams* (Chapman and Hall, London, 1997).

[3] T. Trillo and W. Torruellas, *Spatial Solitons*, (Springer, New York, 2001).

[4] C. S. Gardner et al., *Phys. Rev. Lett.*, **19**, 1095 (1967).

[5] A. Hasegawa and F. D. Tappert, *Appl. Phys. Lett.*, **23**, 142 (1973).

[6] L. F. Mollenauer et al., *Opt. Lett.*, **8**, 289 (1983).

[7] V. Skarka, N. B. Aleksic, H. Leblond, B. A. Malomed and D. Mihalache, *Phy. Rev. Lett.*, **105**, 213901 (2010).

[8] B. A. Malomed, *Soliton Management in periodic systems* (springer, New York, 2006).

[9] F. K. Abdullaev, H. Grammel and da Luz and L. Tornio, *Phy. Rev. A*, **76**, 043611 (2007).

[10] Er'el Granot and B. A. Malomed, *Phy. Rev. B*, **62**, 2185 (2000).

[11] S. Barland, J. R. Tredicce and M. Brambilla, *Phy. Rev. Lett*, **90**, 253903 (2003).

[12] V. Skarka, N. B. Aleksic and H. Leblond, *Acta Physica Polonica A.*, **115**, 5 (2007).

[13] D. Mihalache, F. Lendere, H. Leblond and B. A. Malomed, *Phy. Rev. A*, **75**, 033811 (2007).

[14] K. Aysha Muhsina and P. A. Subha, *Physica Scripta*, **89**, 075205 (2014).

Level Density parameters of Thorium isotopes spanned between drip lines

Ummukulsu E and Antony Joseph
Department of Physics, University of Calicut, Malappuram, Kerala -673635.

Abstract

Total level densities are important key factors in the statistical calculation of many physical processes in diverse fields including from nuclear medicine and astrophysics. The present work is a theoretical study of the effective and collective nuclear level density parameter of thorium nuclei from the proton drip line to neutron drip line. These evaluated data are useful for understanding the nuclear reactions taking place in nucleosynthesis under extreme conditions. The values of effective and collective level density parameter decrease towards the neutron magic numbers N=126 and 184 and towards the drip lines.

1 Introduction

Total level densities are important key factors in the statistical calculation of many physical processes in diverse areas including nuclear medicine and astrophysics. The evaluation of the level density parameter is important as it plays a major role in the determination of nuclear level density. It is important in the estimation of nuclear reaction rates in nuclear physics. The experimental value of the level density parameter is available by analysing evaporation spectra and the neutron resonance spacing [1]. Calculation of nuclear level density parameters for the isotopes of thorium will be helpful in the investigation of reaction cross-sections.

In general nuclei have very closely spaced levels away from the ground state and it is usual to describe the levels in terms of level densities. The number of energy levels per unit energy at any excitation energy E_x is the nuclear level density (NLD). The level density parameter is the important ingredient for the calculation of nuclear level density. The present work is a theoretical study of the effective and collective nuclear level density parameter of thorium nuclei distributed from the proton drip line to neutron drip line. These evaluated data are useful for understanding the nuclear reactions taking place in nucleosynthesis under extreme conditions.

2 Theory

Bethe introduced the concept of nuclear level density in 1936, based on the Fermi gas model[2]. NLD has been extensively studied, using both phenomenological [3] as well as microscopic models. All phenomenological expressions of level density at high excitation energies follow a Fermi Gas expression, which mainly depend on the level density parameter (a). Two types of approaches are followed in estimating it, depending on whether the collective effects are considered or not. If the collective effects are not explicitly included, we get the effective level density (ELD) and if they are included, we get the collective level density (CLD).

The Fermi gas level density $\rho_F(E_x, J)$ for a given spin J at excitation energy E_x is given by,

$$\rho_F(E_x, J) = \frac{1}{2}\left[\frac{(2J+1)\exp\left[-\frac{\left(J+\frac{1}{2}\right)^2}{2\sigma^2}\right]}{2\sigma^2}\right]\left[\frac{1}{\sqrt{2\pi}\sigma}\frac{\sqrt{\pi}}{12}\frac{\exp\left[2\sqrt{aU}\right]}{a^{\frac{1}{4}}U^{\frac{5}{4}}}\right] \quad (1)$$

Ignatyk et.al[4] suggested the shell effect in level density and introduced the pairing effect and energy dependence . The level density parameter a,

$$a(E_x) = \tilde{a}\left[1 + \delta W\frac{1-\exp\left(-\gamma U\right)}{U}\right] \quad (2)$$

$\tilde{a}$ is the asymptotic level density and its value is given by,

$$\tilde{a} = \alpha A + \beta A^{\frac{2}{3}} \quad (3)$$

where α, β and γ are three global parameters, which give the best average value of level density [5]. Different models have different global parameters. Here we consider Gilbert- Cameron model for the calculation of level density parameters. The global parameters used for the present study is tabulated below

Model	α	β	γ
Effective	0.0692559	0.282769	0.433090
Collective	0.0207305	0.229537	0.473625

δW is shell correction energy expressed in MeV and is calculated by using the difference between the experimental mass from the experimental mass compilation [6] and M_{LDM} is the mass according to spherical liquid drop model [7].

$$\delta W = M_{exp} - M_{LDM} \quad (4)$$

3 Results and Discussion

The effective and collective level density parameters for thorium nuclei, with A=194 to 306 is calculated and is plotted in fig 1. The level density parameter strongly depends on the shell correction energy. Experimental level density parameter of ^{230}Th is available [8] and our values are compared with it. Here the collective level density parameter is less than the effective

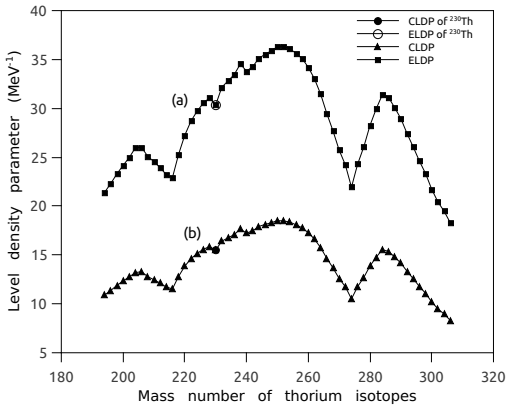

Figure 1: Comparison of effective and collective level density parameter a of Thorium isotopes.

level density parameter. Collective effects arising from the rotational and vibrational degree of freedom loweres the value of level density parameter. Level density parameter decrease towards the neutron magic number N=126 and 184 due to shell closure property.

Here we also calculated the shell correction energy of thorium isotopes spanned between the drip lines. The variation of the shell correction energy with the mass number of thorium isotopes are plotted in fig 2. Variation of shell correction energy and level density parameter shows the same behaviour as can be seen from fig 1 (a) and fig 2. This indicates that the level density parameter significantly depends on the shell correction energy.

4 Conclusion

The effective and collective level density parameter of thorium isotopes spanned between the drip lines are calculated by statistical method, namely, Gilbert-Cameron model. The collective level density parameter is less than the effective level density parameter. Both effective and collective level density parameters decrease towards the neutron magic numbers N=126 and 184 and also towards the drip lines. The shell correction energy and level density parameter for the same mass range show similar behaviour. So it

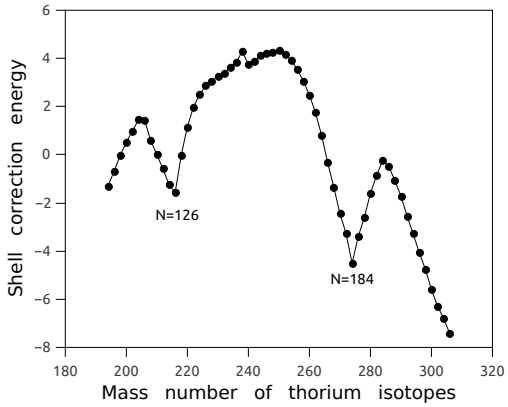

Figure 2: Variation of shell correction energy with mass number of thorium isotopes

can be concluded that the level density parameter strongly depends on shell correction energy.

5 Acknowledgments

Ummukulsu acknowledges the financial support from CSIR under the JRF scheme.

References

[1] A.J. Koning et al.*Nuclear Physics A* **810** 13-76 (2008)

[2] H. A. Bethe, *Rev. Mod. Phys.* **9**, 69 (1937)

[3] A.Gilbert and A.G.W. Cameron, Can.J.Phy.43, 1446-1496 (1965)

[4] A V Ignatuk et al, *Sov. J. Nucl. Phys.* **21**, 255 (1975) .

[5] Albert Mengoni' *J. of Nucl. Sci. and Tech.* **31** 151-162 (1994)

[6] A.H. Wapstra *Nucl. Phys. A* **729** 129–336 (2003)

[7] W.D. Myers and W.J. Swiatecki,*Nucl. Phys. A* **81**, 1-60 (1966).

[8] R. O Owens, *Nuclear Physics A*, **112** 337-359 (1968)

Signatures of secular evolution in nearby early type galaxies

K. Sruthi and C. D. Ravikumar
Department of Physics, University of Calicut, Malappuram, Kerala -673635.

Abstract

We present results of photometric bulge-disc decomposition of 28 nearby (< 30 Mpc) early type galaxies on *Spitzer* images at a wavelength of 3.6 μm. The sample constructed from Swartz et al.(2011, 2004), comprises of 19 ellipticals and 9 lenticulars. We fitted the light profiles of galaxies with two components, a śersic one and an exponential one. Structural parameters of bulge and disc components were evaluated. From our analysis, 14 out of 28 galaxies show presence of discs in them in terms of their B/T ratio. The galaxies showing discs are having large values of disc scale length also. 50% of the galaxies show large scale discs in them in terms of their r_d /r_e ratio. 11 out of 19 ellipticals in the sample show discy nature. This finding is important in the case of ellipticals in our sample as they are thought to be simpler systems with little or no discs or other structural components than other type of galaxies. The bulge effective radius is correlated with the disc scale length. Correlations between bulge and disc radii are not new, and have been used to argue for secular evolution as the primary mechanism of bulge formation. A strong correlation exists between bulge effective radius and disc scale length giving the idea that their formation is coupled. We interpret these results as an evidence for bulge formation by re-distribution of disc material to the centre in agreement with the models of secular evolution in galaxies.

Introduction

Early type galaxies (ETGs) are generally described as red, retired and morphologically featureless systems at the end of galaxy evolution. However, recent studies reveal that, ETGs represent a whole family showing wide range of specific angular momenta [1], bulge to total luminosity ratios [2, 3], cold and ionized gas amounts [4, 5] and star formation modes [6]. The ETGs have long been a misclassified and consequently a misunderstood population. Some of the general ongoing confusion surrounding the ETG population is arising from their treatment as disc-less, one-component systems [14]. Different mechanisms have played significant role in shaping final structure of ETGs even though they were interpreted as the final product of major/minor

merging events [8]. Studying galaxy images, Rix & White (1990) reported that almost all non-boxy "elliptical" galaxies could have discs. Evidences exist for elliptical galaxies generally have complicated dynamical structures and disturbed morphologies. The central studies of early-type galaxies revealed that, many contain discy isophotes which are most likely due to embedded stellar discs. Recent HST observations identified many stellar discs within central kilo parsec that are distinct from outer discs present in lenticular galaxies [9]. As these discs are not simple extensions of the large-scale discs to the centres of galaxies, the origin of these nuclear stellar discs has been a matter of recent debate. The nuclear discs could be the result of the infall of mass to the centre of the galaxy driven by secular evolution [10]. A possible product of such evolution is a formation of bulge-like component having stellar population similar to that of a disc and thus younger than the old spheroid formed by the last major merger [11]. The disc-like properties of bulges and the links between bulge and disc properties have been suggested to indicate that bulges may form through the evolution of disc dynamical in-stabilities such as bars, which are present in about 70% of disc galaxies [12, 13].

Clues to the past evolution of galaxies can be found encoded within their morphologies [14]. The demand for quantitative galaxy morphology met with a wealth of tools which accurately characterize components of galaxies based on their surface brightness distributions [15]. Photometric bulge-disc decompositions in which structural parameters of galaxies are deciphered by disentangling the bulge and disc contributions from their light distribution have long been used as a way of separating out the central and extended components in a galaxy [16]. It has been accepted as an effective tool in unravelling many mysteries associated with galaxy evolution.

In this paper,we report the discovery of exponential discs in elliptical galaxies taken from a sample of early type galaxies using their structural analysis involving photometric bulge-disc decomposition method. To obtain the light distribution of the bulges and discs of each galaxy, we performed bulge-disc decomposition analysis on the images using the code GALFIT [17]. The bulge was modelled using śersic profile [18] and the disc was modelled using an exponential function [19]. The strong correlation exhibited by the bulge effective radius and disc size hints a possible secular evolution happened in the sample.

Sample & Data reduction

Our sample is constructed by selecting all early type galaxies within 30 Mpc with *Chandra* observations and comprises of 19 ellipticals and 9 lenticulars. The morphological types of the galaxies are taken from the RC3 catalogue. However, throughout the paper, we do not attempt to distinguish

the lenticulars, as their sample size is not large enough to convert any result statistically significant. The sample effectively produces a representative set of early-type galaxies within 30 Mpc. Images of galaxies were downloaded from Spitzer Heritage Archive taken using Infra Red Array Camera (IRAC) at 3.6 μm of Spitzer space telescope. Only 10 per cent or even less of the emission in the 4.5 μm band is stellar and that at longer wavelengths the fraction is even lower [20]. So we chose to use 3.6 μm band of IRAC for the present analysis. Basic Calibrated Data (BCD) of the galaxies were downloaded from the archive. The image mosaicking and source extraction package MOPEX [21] was used to co-add BCD frames for each galaxy. Preliminary Surface photometry was done on the images using IRAF task *ellipse*. The Mask file used for this is constructed using SExtractor [22].

Results and Discussion

Exponential discs in the sample

From the two dimensional bulge/disc decomposition analysis of the sample, 14 out of 28 galaxies show presence of discs in them in terms of their B/T ratio. The galaxies showing discs are having large values of disc scale length also. 50% of the galaxies show large scale discs in them in terms of their r_d/r_e ratio. 11 out of 19 ellipticals in the sample show discy nature. This finding is important in the case of ellipticals as they are thought to be simple systems with little or no discs or other structural components. The disc dominance in the sample galaxies is obvious from the histogram of B/T shown in Figure 1. 50% of the sample showing B/T < 0.5 suggesting their discy nature. [23] investigated the photometric signatures of disc components in early-type galaxies concentrating on their isophotal shapes. The superposition of a thin disc and elliptical bulge can give good account for the morphology of most of the early-type galaxies [24]. Rest et al. (2001) studied the central regions of 67 early-type galaxies obtained with WFPC2 camera of HST and found evidence for embedded stellar discs in a remarkably large fraction of 51%. Existence of large rotating discs in early-type galaxies was reported by [25] coupling photometric decomposition with kinematic properties. Figure 3 shows the distribution of ratio of disc scale length to the bulge effective radius in the sample from which it is evident that, the sample is showing large scale discs in their structure.

Correlation between bulge and disc parameters

A strong correlation between bulge and disc properties is interpreted to support secular evolution, as mergers or strong interactions results in destruction of discs and relatively rapid enhancement of bulges. The correlation (linear correlation coefficient r = 0.95, significance > 99.99 %) between

Table 1: Basic galaxy properties.

Galaxy	Distance(Mpc)	Hubble Type	r_e(kpc)	$\triangle r_e$	r_d(kpc)	$\triangle r_d$	r_d/r_e	B/T
IC 1459	26.18	E	1.21	0.05	4.28	0.15	3.55	0.47
NGC 0404	3.86	S0	0.21	0.4	0.35	0.05	1.67	0.28
NGC 0720	24.42	E	1.19	0.01	4.47	0.04	3.75	0.42
NGC 0855	9.28	S0	0.27	0.02	0.88	0.09	3.29	0.36
NGC 1316	19.18	S0	28.31	3.22	2.34	0.07	0.08	0.96
NGC 1399	17.71	E	1.16	0.01	4.2	0.07	3.63	0.43
NGC 1407	24.05	E	2.32	0.05	7.51	0.13	3.24	0.44
NGC 1549	16.57	E	0.97	0.08	2.46	0.05	2.55	0.42
NGC 1553	15.11	S0	7.02	1.8	1.66	0.04	0.24	0.71
NGC 3115	10.28	S0	3.43	0.19	0.19	0.03	0.05	0.97
NGC 3379	11.07	E	3.51	0.09	0.16	0	0.05	0.93
NGC 3585	17.29	E	1.82	0.05	4.98	0.09	2.74	0.54
NGC 3607	21.3	S0	0.91	0.03	2.49	0.1	2.75	0.59
NGC 4111	12.86	S0	0.42	0.02	1.55	0.08	3.7	0.72
NGC 4125	22.76	E	3.81	0.09	7.7	0.42	2.02	0.79
NGC 4365	21.6	E	1.96	0.05	5.51	0.1	2.82	0.53
NGC 4374	16.97	E	1.02	0.04	2.78	0.08	2.74	0.47
NGC 4382	15.28	E	1.12	0.09	2.7	0.02	2.4	0.35
NGC 4472	16.06	E	1.46	0.07	3.97	0.14	2.71	0.4
NGC 4486	16.75	E	1.68	0.02	5.23	0.08	3.12	0.39
NGC 4494	13.64	E	6.57	0.3	1.85	0.05	0.28	0.92
NGC 4552	16.47	E	0.55	0.04	2.44	0.46	4.43	0.76
NGC 4621	16.01	E	2.13	0.28	0.75	0.07	0.35	0.93
NGC 4636	16.3	E	0.95	0.03	4.09	0.14	4.3	0.3
NGC 4649	16.7	E	1.15	0.01	3.99	0.04	3.46	0.37
NGC 4697	12.17	E	14.41	0.73	1.98	0.04	0.14	0.95
NGC 5102	11.99	S0	0.97	0.19	2.79	0.14	2.88	0.5
NGC 5128	3.81	S0	4.06	0.26	8.64	1.51	2.13	0.74

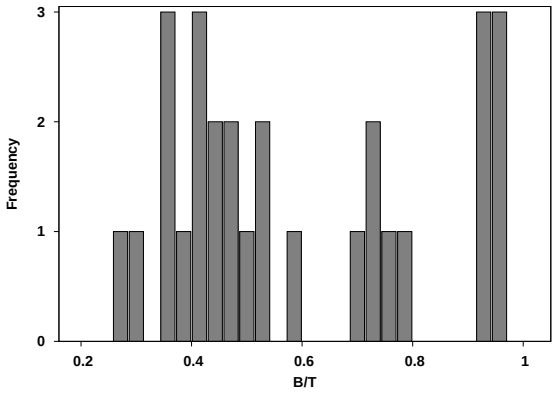

Figure 1: Distribution of B/T ratio of sample galaxies.

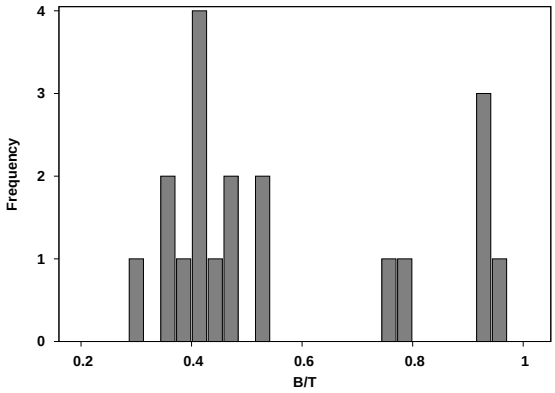

Figure 2: Distribution of B/T ratio of ellipticals in the sample.

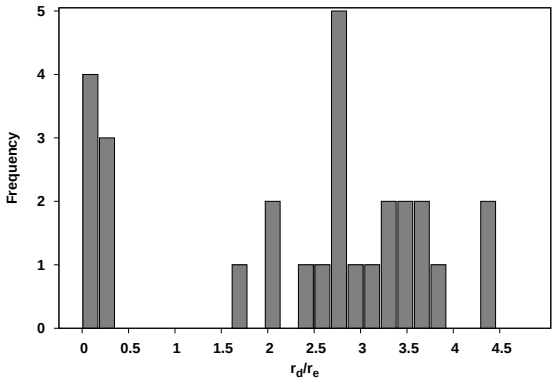

Figure 3: Distribution of r_d/r_e ratio of galaxies.

bulge effective radius and the disc scale length of the sample shown in Figure 4, is giving the idea that their formation of bulges and discs is coupled.

Seven galaxies (NGC 1316, NGC 1553, NGC 3115, NGC 3379, NGC 4494, NGC 4621, NGC 4697) in the sample show deviation from the trend. Presence of additional structures visible in their residual images obtained from the analysis may be the possible reason for their deviation. But in the case of the galaxy NGC 1316, the ongoing merging with the neighbour cause a bad fitting. Correlations between bulge and disc radii are not new, and have been used to argue for secular evolution as the primary mechanism of bulge formation. This correlation shown by the sample hints at the role of secular evolution happened in them. The bulge is expected to be formed from the disc by secular evolution. In galaxy discs, gas in-fall and star formation builds dense central components that could be mistaken for bulges formed by galaxy mergers. They come in several varieties depending on what drives the evolution.

Conclusion

From the analysis of a representative sample of early-type galaxies, we report the existence of exponential disc components in elliptical galaxies. The effective radius of the bulge component is strongly correlated with the size of the disc component. These results show that, the discs obeying exponential law in the sample are formed through recent secular evolution processes. After the initial collapse and major merger events, the sample may undergo gradual re-arrangement in their structure via internal instabilities. Environment may play a crucial role in growing discs in their structure.

Acknowledgements

I greatly acknowledge ***DST-INSPIRE*** for my research fellowship. We acknowledge the use of the NASA Extragalactic Database (NED), https://ned.ipac.caltech.edu/ operated by the Jet Propulsion Laboratory, California Institute of Technology.

References

[1] Cappellari. M et al., *MNRAS*, **416**, 1680(2011).

[2] J. Kormendy and R. Bender, *ApJS*, **198**, 2(2011).

[3] Méndez-Abreu et al., *MNRAS*, **474**, 1307(2018).

[4] Serra. P et al., *MNRAS*, **422**, 1835(2012).

[5] Davis. T. A et al., *MNRAS*, **417**, 882(2011).

[6] Shapiro. K. L et al., *MNRAS*, **402**, 2140(2010).

[7] Graham. A. W et al., *MNRAS*, **487**, 4995(2019).

[8] Longhetti. M, Bressan. A, Chiosi. C, and Rampazzo. R, *AAP*, **353**, 917(2000)

[9] Lopes. R. D. S, Storchi-Bergmann. T, de Fatima Saraiva. M., and Martini. P, *ApJ*, **655**, 718(2007).

[10] Krajnović, D. and Jaffe. W, *AAP*, **428**, 877(2004).

[11] Debattista. V. P, Mayer. L, Carollo. C. M, Moore. B, Wadsley. J, and Quinn. T, *ApJ*, **645**, 209 (2006).

[12] Knapen, J. H. *Observations of Barred Galaxies, volume of Astronomical Society of the Pacific Conference Series*, **187**, 72(1999).

[13] Eskridge P. B. et al., *The Frequency of Barred Spiral Galaxies in the Near-Infrared.* , **119(2)**, 536–544(2000).

[14] Graham. A. W, *MNRAS*, **487**, 4995(2019).

[15] Bottrell. C, Simard. L, Mendel. J. T, and Ellison. S. L, *MNRAS*, **486**, 390(2019).

[16] Tabor. M et al., *MNRAS*, **485**, 1546(2019).

[17] Peng. C. Y, Ho. L. C, Impey. C. D., and Rix. H.-W. *Detailed Structural Decomposition of Galaxy Images*, **124(1)**, 266–293(2002).

[18] Sersic. J. L, *Atlas de Galaxias Australes*, (1968).

[19] Freeman. K. C, *On the Disks of Spiral and S0 Galaxies*, 160:811, (1970).

[20] Leitherer. C, et al., *Starburst99: Synthesis Models for Galaxies with Active Star For- mation*, **123**(1):3–40, (1999).

[21] Makovoz. D, and Marleau. F. R, *Point-Source Ex- traction with MOPEX*, **117**(836):1113–1128, (2005).

[22] Bertin. E, and Arnouts. S, *SExtractor: Software for source extraction*, **117**, 393–404(1996).

[23] Rix. H.-W, and White. S. D. M, *Disks in Elliptical Galaxies*, **362**, 52(1990).

[24] Scorza. C, *Stellar disks and em- bedded bars in early-type galaxies. I. 2-D photometric decomposition of 28 southern early-type galaxies*, **131**, 265–286, (1998).

[25] Krajnovi. D et al., *MNRAS*, **432(3)**, 1768(2013).

Alpha and Cluster decay using MGLDM with cluster size dependent preformation factor

Tinu Ann Jose and K. P Santhosh
School of Pure and Applied Physics, Kannur University, Payyanur 670327

Abstract

Alpha and cluster decay from various radioactive parent nucleus are studied using Modified Generalized Liquid Drop Model (MGLDM) with new preformation factor. Preformation factor used depends on cluster size or mass number of emitted cluster is used. MGLDM is an approach proposed by Santhosh et al., by adding proximity potential 77 to existing Generalized liquid drop model (GLDM). Both alpha and cluster decay half-lives are computed using MGLDM with cluster size dependent preformation factor and is compared with experimentally observed half-lives. We could reproduce experimental half-lives in case of both alpha decay and cluster decay with an overall standard deviation of 0.58. We predict half-lives of various clusters emitted from radioactive Np, Pu, Am parent nuclei and compares it with the predictions made by Bao et al.,.[J. Phys. G: Nucl. Part. Phys. **39**,095103(2012)] We hope that our present study would be helpful when such elements are detected in near future.

Introduction

The process of cluster emission, the decay process by which, emitted particle has mass greater than alpha particle and lighter than fission fragments was predicted for the first time by Sandulescu et al.,[1] in 1980. Rose and Jones[2] experimentally confirmed this prediction in 1984 where ^{14}C was found to be emitted from ^{223}Ra. Later emission of other clusters like ^{20}O, ^{23}F, ^{22,24,26}Ne, ^{28,30}Mg, ^{32,34}Si were confirmed experimentally[3, 4].

Alpha decay and cluster emission are found to be the main radioactive decay mechanism from heavy parent nuclei. Many theoretical models are proposed by nuclear physicist to explain the underlying principle and theories behind such decay process. Preformed Cluster Model (PCM)[5, 6] and Unified Fission Model (UFM)[7, 8] are major two theoretical models that explain alpha and cluster decay.

Royer[9, 10] in 1984, proposed Generalized Liquid Drop Model (GLDM) which included quasi-molecular shape and nuclear proximity energy to conventional Liquid Drop Model (LDM). Santhosh et al.,[11] modified GLDM

of Royer by including proximity potential proposed by Blocki et al.,[12] and the model is named as Modified Generalized Liquid Drop Model (MGLDM). Again in our previous work[13] we have included cluster size dependent preformation factor to MGLDM and the standard deviation obtained for both cluster and alpha decay is 0.58. Hence in our present paper, we predict the half-lives of various clusters emitted from Np, Pu and Am parent nuclei.

Present paper is organised as follows: Section 2 contains the theory of MGLDM. Section 3 contains the result and discussion. Section IV summarizes the entire work.

Theory

In MGLDM, for a deformed nucleus, the macroscopic energy is defined as,

$$E = E_V + E_S + E_C + E_R + E_P \tag{1}$$

Here the terms E_V, E_S, E_C, E_R and E_P represents the volume, surface, Coulomb, rotational and proximity energy terms respectively. For the prescission region the volume, surface and Coulomb energies in MeV are given by,

$$E_V = -15.494(1 - 1.8I^2)A \tag{2}$$

$$E_S = 17.9439(1 - 2.6I^2)A^{2/3}(S/4\pi R_0^2) \tag{3}$$

$$E_C = 0.6e^2(Z^2/R_0)X0.5\int(V(\theta)/V_0)(R_0/R_0)^3 sin\theta d\theta \tag{4}$$

Here I is the relative neutron excess and S the surface of the deformed nucleus, $V(\theta)$ is the electrostatic potential at the surface and the surface potential of the sphere.

For the post-scission region,

$$E_V = -15.494[(1 - 1.8I^2)A_1 + (1 - 1.8I^2)A_2] \tag{5}$$

$$E_S = 17.9439[(1 - 2.6I^2)A^{2/3} + (1 - 2.6I^2)A^{2/3}] \tag{6}$$

$$E_C = \frac{1.6e^2Z_1^2}{R_1} + \frac{1.6e^2Z_2^2}{R_2} + \frac{e^2Z_1Z_2}{r} \tag{7}$$

Here A_i, Z_i, R_i and I_i are the masses, charges, radii and relative neutron excess of the fragments, r is the distance between the centers of the fragments.

The nuclear proximity potential is given by Blocki et al.[12] as,

$$V_p(z) = 4\pi\gamma b[\frac{C_1C_2}{C_1 + C_2}]\Phi(\frac{z}{b}) \tag{8}$$

With the nuclear surface tension coefficient,

$$\gamma = 0.9517[1 - 1.7826(N - Z)^2/A^2]MeV/fm^2 \tag{9}$$

where N, Z and A represent neutron, proton and mass number of parent nucleus respectively,represents the universal proximity potential[14] given as,

$$\Phi(\varepsilon) = -4.41e^{-\varepsilon/0.7176}, for\ \varepsilon > 1.9475 \tag{10}$$

$$\Phi(\varepsilon) = -1.7817 + 0.9270\varepsilon + 0.0169\varepsilon^2 - 0.05148\varepsilon^3,\ for\ 0 \leq \varepsilon \leq 1.9475 \tag{11}$$

with $\varepsilon = z/b$, where the width (diffuseness) of the nuclear surface b $\approx$ 1 fm and Süsmann central radii C_i of fragments related to sharp radii R_i as,

$$C_i = R_i - \frac{b^2}{R_i} \tag{12}$$

For R_i we use semi empirical formula in terms of mass number A_i as[14],

$$R_i = 1.28A_i^{1/3} - 0.76 + 0.8A_i^{-1/3} \tag{13}$$

The barrier penetrability P is calculated with the action integral

$$P = \exp\left\{ -\frac{2}{\hbar} \int_{R_{in}}^{R_{out}} \sqrt{2B(r)\left[E(r) - E(sphere)\right]}dr \right\} \tag{14}$$

Where $R_{in} = R_1 + R_2$, $B(r) = \mu$ and $R_{out} = \frac{e^2 Z_1 Z_2}{Q}$. R_1, R_2, are the radius of the daughter nuclei and emitted cluster respectively, and the reduced mass and the released energy.

The partial half-life is related to the decay constant by

$$T_{1/2} = \frac{ln\ 2}{\lambda} = \frac{ln\ 2}{\nu P_c P} \tag{15}$$

The assault frequency has been taken as $10^{20}s^{-1}$. P_c is the pre-formation factor.

Preformation probability plays an important role in determining half-life in the case of both cluster and alpha decay. In our present approach, we assume cluster to be preformed within parent nuclei before being emitted and tunnel through potential barrier. Again we calculated the dependence of experimentally extracted preformation factor on mass number of emitted cluster. We got a linear dependence. Hence our group formulated an equation for preformation factor that dependence on cluster size and is given as:

$$P_c = 10^{aA_c + b} \tag{16}$$

Where A_C is the mass number of cluster, and parameters a and b is obtained by least square fitting method with experimental values, with $a = -0.51325$ and $b = 2.80787$.

Table 1: Prediction of half-lives of various clusters from Np, Pu. Am Parent nuclei.

Parent Nuclei	Emitted Cluster	Daughter nuclei	Q(MeV)	$log_{10}T_{1/2}$	
				MGLDM	Bao
^{225}Np	^{12}C	^{213}Fr	35.26	9.96	10.38
^{225}Np	^{16}O	^{209}At	49.37	14.24	14.72
^{227}Np	^{16}O	^{211}At	49.11	14.49	15.28
^{227}Np	^{18}O	^{209}At	46.39	20.69	21.00
^{231}Np	^{20}O	^{211}At	43.64	20.01	28.23
^{233}Np	^{22}Ne	^{211}Bi	58.03	26.55	27.97
^{233}Np	^{25}Ne	^{208}Bi	59.08	2.62	27.81
^{234}Np	^{28}Mg	^{206}Tl	77.46	22.49	22.72
^{235}Np	^{29}Mg	^{206}Tl	74.13	27.48	28.04
^{236}Np	^{29}Mg	^{207}Tl	75.24	25.89	26.49
^{237}Np	^{31}Si	^{205}Au	88.12	2.67	28.26
^{225}Np	^{14}C	^{211}Fr	32.83	16.70	16.49
^{227}Np	^{14}C	^{213}Fr	33.22	15.85	16.08
^{227}Np	^{17}O	^{210}At	45.50	21.08	22.11
^{229}Np	^{18}O	^{211}At	46.37	20.60	21.26
^{231}Np	^{22}Ne	^{209}Bi	62.10	20.73	21.11
^{234}Pu	^{27}Na	^{207}Bi	66.14	29.2	30.86
^{234}Pu	^{29}Al	^{205}Tl	82.63	26.36	27.15
^{236}Pu	^{24}Ne	^{212}Po	59.42	27.35	28.57
^{236}Pu	^{29}Al	^{207}Tl	82.40	26.49	27.71
^{237}Pu	^{29}Mg	^{208}Pb	77.68	24.07	23.83
^{237}Pu	^{32}Si	^{205}Hg	91.73	24.95	25.00
^{234}Pu	^{24}Ne	^{210}Po	62.45	22.94	23.46
^{234}Pu	^{28}Mg	^{206}Pb	79.39	21.51	21.73
^{234}Pu	^{32}Si	^{202}Hg	92.04	24.86	24.26
^{236}Pu	^{27}Na	^{209}Bi	66.89	28.44	28.91
^{236}Pu	^{32}Si	^{204}Hg	91.93	24.80	24.68
^{237}Am	^{28}Mg	^{209}Bi	80.09	21.80	21.89
^{237}Am	^{32}Si	^{205}Tl	94.74	23.06	23.00
^{238}Am	^{29}Mg	^{209}Bi	77.52	25.64	25.82
^{238}Am	^{33}Si	^{205}Tl	93.03	25.53	25.48
^{239}Am	^{32}Si	^{207}Tl	94.78	22.84	23.11
^{239}Am	^{34}Si	^{205}Tl	93.44	25.58	25.28
^{240}Am	^{34}Si	^{206}Tl	93.99	24.85	24.66
^{241}Am	^{34}Si	^{207}Tl	94.20	24.52	24.41
^{237}Am	^{29}Mg	^{208}Bi	76.28	27.37	27.52
^{238}Am	^{28}Mg	^{210}Bi	78.47	23.71	24.15
^{238}Am	^{32}Si	^{206}Tl	95.03	22.65	22.73
^{239}Am	^{30}Mg	^{209}Bi	76.78	27.25	27.32
^{239}Am	^{33}Si	^{206}Tl	92.43	26.15	26.40
^{240}Am	^{33}Si	^{207}Tl	93.33	25.01	25.28
^{241}Am	^{33}Si	^{208}Tl	90.47	28.32	29.15

Results and Discussion

In our previous work, we have studied cluster and alpha decay from parent nuclei in trans-lead region using MGLDM with different preformation probabilities[13]. Three types of preformation probabilities that depend on cluster size, Q value and atomic number of cluster and daughter nuclei were used. Half-lives computed are compared with the experimental half-lives and the minimum standard deviation is obtained for MGLDM with cluster size dependent preformation factor. Hence in present work, half-lives of different clusters emitted from heavy parent nuclei like Neptunium, Plutonium and Americium with atomic number 93-95 are predicted using MGLDM with cluster size dependent preformation factor. Logarithms of half-lives calculated are listed in Table 1. The predicted values are compared with the prediction made by Bao et al.,[15] and it is very clear that both the predictions are comparable. So with no doubt, one can conclude that MGLDM with cluster size dependent preformation probability is a good theoretical approach to study both cluster and alpha decay.

Conclusion

Cluster decay from heavy parent nuclei with atomic number 93-95 are predicted using MGLDM with cluster size dependent preformation factor. As we are able to replicate experimentally observed values using our model in previous work, we hope that this predictions would be very helpful in future for studies in this field.

Acknowledgments

One of the authors (KPS) would like to thank the Government of Kerala, India for the financial support in the form of Research Project under Innovative Research Programme.

References

[1] A Sandulescu, D N Poenaru and Greiner W, *Sov. J. Part. Nucl*, 11 528 (1980)

[2] H J Rose and G A Jones, *Nature*, 307 245 (1984)

[3] R K Gupta and W Greiner, *Int. J. Mod. Phys.E*, 3 335 (1994)

[4] Yu S Zamyatnin, V L Mikheev, S P Tret'yakova, V I Furman, S G Kadmenskii and Yu M Chuvil'skii, *Sov. J. Part. Nucl*, 21 231 (1990)

[5] S Kumar, MBalasubramaniam, R K Gupta, G Münzenbergand W Scheid, *J. Phys. G: Nucl. Part. Phys*, 29 625 (2003)

[6] S Kumar, R Rani and R Kumar, *J. Phys. G: Nucl. Part. Phys*, 36 015110 (2009)

[7] D N Poenaru, M Ivascu, A Sandulescu and W Greiner, *Phys. Rev. C*, 32 572 (1985)

[8] Y J Shi and W J Swiatecki, *Nucl. Phys. A*., 464 205 (1987)

[9] G. Royer and B. J. Remaud, *J. Phys. G: Nucl. Part. Phys.*, 10 1057 (1984).

[10] G. Royer and B. Remaud, *Nucl. Phys.A*, 444 477 (1985).

[11] K. P. Santhosh,C. Nithya,H. HassanabadiandDashty T. Akrawy, *Phys. Rev.C*, 98, 024625 (2018).

[12] J. Blocki, J. Randrup, W. J. Swiatecki, and C. F. Tsang, *Ann. Phys. (NY)*, 105, 427 (1977).

[13] K. P. Santhosh, Tinu Ann Jose, *Indian Journal of Physics*(communicated).

[14] J Blocki and W J Swiatecki, *Ann. Phys. (NY)*, 132, 53 (1981)

[15] X. J. Bao, H. F. Zhang, B. S. Hu, G. Royer and J. Q. Li, *J. Phys. G: Nucl. Part. Phys.*, 39, 095103(2012).

Synthesis of Metal Halide Perovskites for Energy Harvesting Applications

Rajita Ramanarayanan* , Kailashnath P.H
Department of Physics, S.A.R.B.T.M Government College,Koyilandy,
Kozhikode, Kerala-673305

Abstract

This investigation aims at the synthesis of a lead free metal halide perovskite material which is a very trending material in the photovoltaic energy conversion scenario. We have synthesized $KCuCl_3$ nanoparticles using wet chemical synthesis at a moderate temperature in this report. The obtained sample was characterized by X-Ray Diffraction (XRD), Scanning Electron Microscope(SEM) and EDAX measurements. The synthesized material showed nanorod morphology showing 1 Dimensional structure which has various potential applications not only as light absorber but also as a charge transporting medium in optoelectronic and photovoltaic devices.

Introduction

The need for energy has been a driving force for human civilisation since time immemorial starting from the discovery of fire. With the passage of time fossil fuels occupied the centre stage leading to tremendous achievements in improving the standard of living of the common man. The scarcity of fossil fuels and the increasing pollution rates due to green house emissions have forced the scientific world to look for alternate sources of energy .Due to the ever growing demands and exploding population energy shortage has been a serious topic of discussion among academicians and social scientists in the last few decades worldwide. India with its fast growing economy and population faces a tough challenge and a great opportunity to successfully explore various non-conventional sources of energy like solar, wind, biomass, geothermal, tidal etc. Among the nonconventional energy resources only solar and wind energy have lead to wide commercial applications. Inspite of these advances wind energy suffers from serious limitations of high installation cost and proper geographical location to facilitate efficient energy conversion. Hence the responsibility for providing clean and green energy everywhere solely rests on solar energy due to its abundant availability. The rate of energy received by the earth from solar energy is approximately 3x 1024 joules which is sufficient to fulfil the growing energy demands[1].

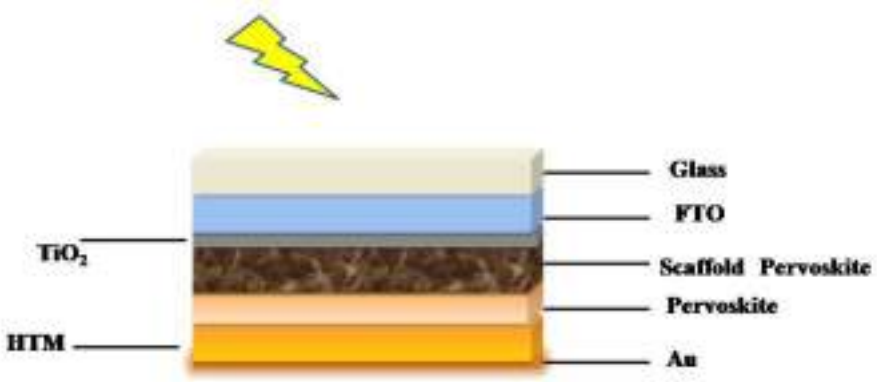

Figure 1: Structure of a Perovskite Solar Cell

India, by virtue of its favourable location near tropic of cancer is blessed with ample amount of sunlight throughout the year. India receives solar energy about 5000 trillion kWh per year with 2300–3200 hours of sun shine in most parts of India which on proper utilisation is sufficient enough to solve the present energy crisis[2]. The effective utilisation of natural resources particularly sunlight for energy harvesting applications is an active area of research for the past few decades. The two prominent methods of light harvesting are photovoltaics and photocatalysis. Though both depend on the electron –hole generation, the electron –hole pairs are driven in a circuit to get current in photovoltaics whereas they participate in a redox reaction in photocatalysis. The discovery of photocatalysis is credited to Fujishima and Honda for their path breaking discovery of photocatalytic splitting of water on TiO2 electrode under ultraviolet light[3].

Photocatalysis is defined as a process where light and the catalyst interact with each other to drive a chemical reaction. The photocatalysis involves the generation of excited electrons in a catalyst (metal, semiconductor and metal-semiconductor) with simultaneous generation of holes upon illumination by light. The photoexcited electrons and holes induces formation of highly reactive hydroxyl ions whose interaction with organic compounds in water/air form biodegradable products[4]. Photocatalysis is responsible for a variety of applications like water/air purification, hydrogen evolution, anti-bacterial and anti-fogging studies[5].

Perovskites are one of the most promising and efficient low-cost energy materials for new generation optoelectronic and photonic devices. The name perovskite originated from the discovery of calcium titanate ($CaTiO_3$) in 1839 by a Russian mineralogist Perovski. The materials with the similar structure crystal of $CaTiO_3$ are known as the perovskite materials[6]. ABX_3 is the general chemical formula used for perovskite materials where

A and B are cations with size of A larger than that of B and X is the anion usually oxides or halogens. The perovskite materials possess unique physical properties such as high-absorption coefficient, high dielectric constant and ferroelectric properties generating huge interest for application of these materials in new generation devices. The two major classes of perovskite materials are chalcogenide perovskite (AMO_3) and halide perovskite (ABX_3). Metal halide perovskites have attracted attention from the research community worldwide due to their applications in solar cells, lasers, light emitting diodes (LED) water splitting and sensing applications[7].These Perovskites are the recent front runners of solar cell technology as shown in Fig.1 showing promising efficiencies comparable to silicon solar cells. Perovskite structures come in various architectures depending on the nature of the perovskite layer that is as light absorbing layer or e^-/h^+ transport layer. The most popular metal halide perovskites are cesium lead halide ($CsPbX_3$) and methylammonium lead halide ($CH_3NH_3PbX_3$) perovskites which have shown good optical and electrical properties. However the use of lead in perovskite components leads to serious environmental concerns and the need for lead free metal halide perovskites has prompted the use of various elements like Copper in place of Lead. In this perspective, we aim to synthesize a lead free metal halide perovskite potassium copper chloride ($KCuCl_3$) nanoparticles using a simple cost effective wet chemical method.

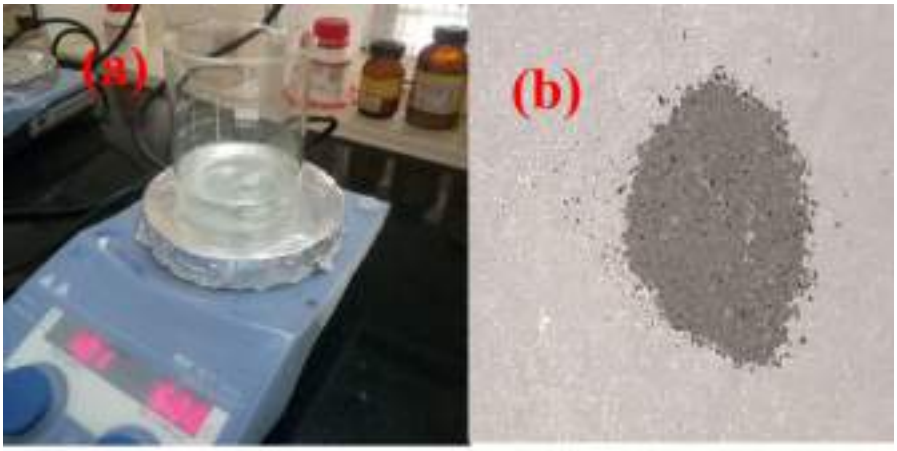

Figure 2: (a) Synthesis (b) dried precipate

Materials and Methods

Preparation Of Potasium Chloride Solution

5mM of KCl solution is prepared according to the following calculations:
molecular weight of KCl=74.55gm
mass of KCl to be taken=$\frac{74.55\times5mM\times100}{100}$ = 0.0372759 gm to be dissolved in 100 ml

Preparation Of Copper Chloride Solution

5mM $CuCl_2$ solution is prepared according to the following calculations:
molecular weight of $CuCl_2$=170.48gm
so,as calculated above
mass of $CuCl_2$=$\frac{170.48x5mMx100}{1000}$ =0.08524gm in 100 ml

At first 5 m M of KCl solution is prepared by taking 0.0372759 gm of KCl in 100 mL of water. Then we prepare 1.1M of HCl solution. After the mixing the above two we add 5 m M of $CuCl_2$ solution to the mixture of KCl and HCl. Then we heat at 100 degrees and stir it for about 60 minutes on a hot plate (IKA Basic). NaOH solution is slowly added drop by drop to the solution till the pH becomes 9.The precipitate formation is observed on addition of NAOH which afterwards is cooled allowing the precipitate to settle down. The precipitate is washed using distilled water and ethanol for 4 times and then we centrifuged at 10,000rpm. After the supernatant is removed the slurry is transferred to a petridish and placed in the oven for drying at 60 degrees for about 5 hours. After drying, greyish black coloured powder obtained is used for further characterizations.

Optical and Electrical Characterisation

X –ray diffraction (XRD) measurements were performed using Rigaku Miniplex–X Ray Diffractometer with monochromatic $Cu-K\alpha$ radiation ($\lambda = 1.54A^{\circ}$), scanned in the 2θ range of 10° to 80°. Surface morphology of the films and composition was obtained via SEM imaging and EDS mapping obtained from Scanning Electron Microscope (Zeiss Gemini SEM 300).

Results and Discussion

X-Ray Diffraction (XRD)

The phase and crystallinity of the synthesized sample were investigated by the XRD patterns. The XRD of synthesized $KCuCl_3$ nanoparticles are shown below in Fig.3. The diffraction pattern is in the agreement with the standard X-ray diffraction peaks (JCPDS no is $72-0261$) confirming that the synthesized material is $KCuCl_3$ monoclinic.

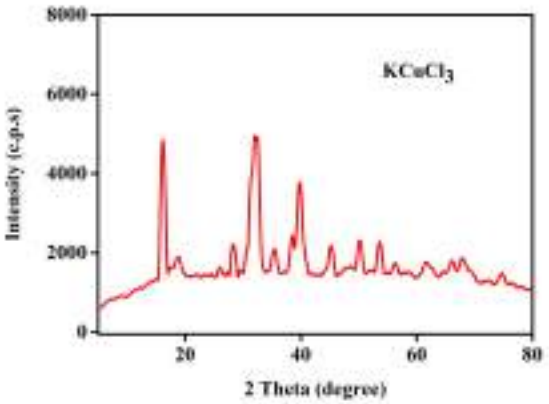

Figure 3: XRD analysis

SEM Analysis

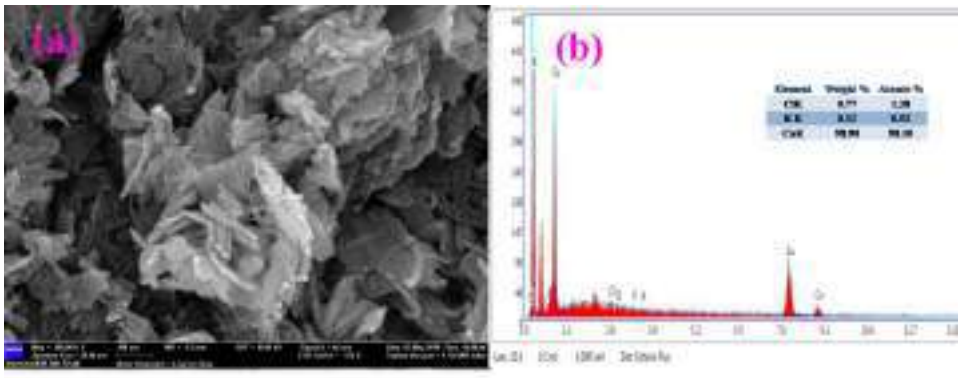

Figure 4: (a) SEM analysis of synthesized sample (b) EDAX of the synthesized sample

SEM analysis was conducted to get information about the size and surface morphology of the synthesized sample. The SEM analysis shows one dimensional structures with width of 11nm and length 150 nm. Though distribution is uniform the nanoparticles are slightly agglomerated which requires further studies in design protocol.

The distribution of the K, Cu and Cl in the compound was examined by EDAX mapping. The EDAX analysis shows the presence of the elements K,Cu,Cl in agreement with the XRD analysis.

Conclusion

We have synthesized a novel lead free metal halide perovskite and conducted SEM, EDAX and XRD characterisations. From XRD characterisations it is confirmed that the sample is $KCuCl_3$. From SEM analysis we see one dimensional rod like structures which are slightly agglomerated. EDAX measurements confirm the presence of K, Cu and Cl. Finally a good light harvesting material has been synthesized using a simple lab method which can be used in a variety of photovoltaic and photocatalysis applications.

Acknowledgments

The authors acknowledge Dr Sindhu.S, Head of the Department of Nanoscience and Technology, University of Calicut for her valuable inputs and permission to use her lab for the synthesis purposes. Authors also thank Central Sophisticated Instrumentation Facility (CSIF) Calicut University for SEM and EDAX analysis.

References

[1] M. Grätzel, Photoelectrochemical cells, *Nature* 414 (2001) 737–740.

[2] S.K. Gupta, R.S. Anand, Development of Solar Electricity Supply System in India: An Overview, *J. Sol. Energy*, 2013 (2013).

[3] A. Fujishima, K. Honda, Electrochemical photolysis of water at a semiconductor electrode, *Nature*, 238 (1972) 37–38.

[4] R. Saravanan, F. Gracia, A. Stephen, Basic Principles, Mechanism, and Challenges of Photocatalysis, in: Nanocomposites Visible Light. *Photocatal.*, Springer, 2017 19–41.

[5] Bhabhina. N. M, Rajita. R, Sindhu. S, Surface modification of oxygen-deficient ZnO nanotubes by interstitially incorporated carbon: a superior photocatalytic platform for sustainable water and surface treatments, *Appl. Nanosci.* (2018) 1–11.

[6] Resmi Verma, Pervoskite Photovoltaics, Elsevier 2018, 1-280.

[7] Son-Tung Ha, Rui Su, Jun Xing, Qing Zhang, Qihua Xiong, Metal halide perovskite nanomaterials: synthesis and applications, *Chem. Sci.* 8 (2017) 2522-2536.

[8] Po Lu, Min Lu, Hua Wang, Ning Sui, Zhifeng Shi, William W. Yu , Yu Zhang,Metal halide perovskite nanocrystals and their applications in optoelectronic devices, *Info Mat.* 1 (2019) 430–459.

[9] Ajay Kumar Jena, Ashish Kulkarni, Tsutomu Miyasaka, Halide Perovskite Photovoltaics: Background, Status, and Future Prospects, *Chem. Rev.* 119(2019) 3036-3103.

[10] Wanchun Xiang, Wolfgang Tress, Review on Recent Progress of All-inorganic Metal Halide Perovskites and Solar Cells, *Adv. Mater.* 1902851 (2019) 1-28.

Structural and morphological studies of substituted copper chromate nanoparticles

K V Shilna[1] and E M A Jamal[2]
[1]Department of Physics, Central University of Kerala, Kasaragod, Kerala
[2]Department of Physics, MHES College of Science and Technology, Vadakara, Kerala

Abstract

Copper chromte ($CuCrO_2$) based delafossite materials attracts great attention due to its promising applications because of its layered structure. In this work, $Cu_{1-x}Ni_xCrO_2$ were synthesized by sol-gel method and the prepared powder samples were annealed at $800°C$. The study considered impact of high concentration nickel substitution on copper chromate nanoparticles using X-ray powder diffraction (XRD), Fourier transform infrared spectroscopy (FTIR) and Scanning electron microscopy (SEM). XRD spectra revealed the formation of $CuCrO_2$ phase as a major product with some peaks corresponding to $CuCr_2O_4$. FTIR spectra showed peaks representing copper chromate. Scanning electron micrographs with different magnification were illustrated.

Introduction

Delafossite oxides have attracted much interest owing to their immense technological applications. These ABO2 metal oxides, where A = Cu, Ag and B = Al, Cr, Ga, In, La, Y, B, etc. can have properties such as p-type transparent conducting, thermoelectric, catalytic, photocatalytic, sensing etc[1, 2, 3, 4, 5, 6, 7]. Transparent conducting oxide (TCO) material combines the properties of electrical conductivity and optical transparency in a single material.

Among several delafossite compounds, $CuAlO_2$ and $CuCrO_2$ are generally characterized as p-type TCOs[8, 9]. In 2001 p-type conductivity was discovered in $CuAlO_2$, since then p-type TCOs have gained better acceptability due to its significant electrical conductivity and transparency. $CuCrO_2$ has also shown p-type TCO properties with lowest resistivity in Mg-doped $CuCrO_2$ films[9]. Generally, these compounds were synthesized by solid-state, hydrothermal, self-combustion, co-precipitation and sol–gel approaches. $CuCr_{1-x}Rh$ x O_2[10] were obtained by chromium substitution in $CuCrO_2$ by the solid state method and $CuCr_{1-x}Mn_xO_2$[11] thinfilms were also prepared by the chemical solution deposition method. S Y Zheng

et.al. reported the nickel (Ni) substituted copper chromate $CuCr_{1-x}Ni_xO_2$[12]. In our case, Ni^{2+} substituted at higher concentrations in $CuCrO_2$ ($Cu_{1-x}Ni_xCrO_2$, $x = 0.25$ and 0.5) was synthesized by the sol-gel method and its structural and morphological properties were studied.

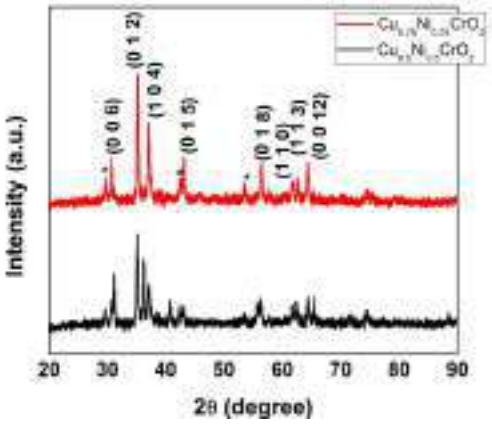

Figure 1: XRD spectra of the $Cu_{1-x}Ni_xCrO_2$ samples annealed at 800°C.

Experimental Methods

Samples were synthesized by sol-gel technique. Reactant materials copper nitrate, Chromium nitrate and Nickel nitrate were weighed according to the stoichiometric ratio. The reactants were added into the ethylene glycol and stirred. This homogeneous solution was heated at 60°C upto gel formation and then to 150°C. All powder samples were annealed at 800°C for 3 hours. X-ray diffraction (XRD) was carried out with Rigaku Miniflex Japan X-ray diffractometer ($CuK\alpha, \lambda = 1.54060A°$) and the phase composition of powder samples were confirmed. Fourier transform infrared spectroscopy (FTIR) studies of the samples were also done. To study the morphological property of the samples scanning electron microscopy (SEM Model: JEOL Model JSM - 6390LV) was carried out.

Results and Discussion

Figure 1 shows the XRD patterns of the $Cu_{1-x}Ni_xCrO_2$ (x = 0.25, 0.5) samples. Obtained XRD patterns were compared with standard ICDD data and indexed to be $CuCrO_2$ as the main phase with the stronger intensity. But there were some impurity peaks observed corresponding to the $CuCr_2O_4$ spinel crystalline phase. With the increasing concentration of

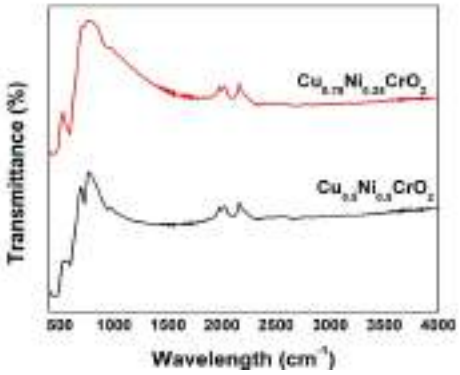

Figure 2: FTIR spectra of the $Cu_{1-x}Ni_xCrO_2$ samples annealed at 800°C.

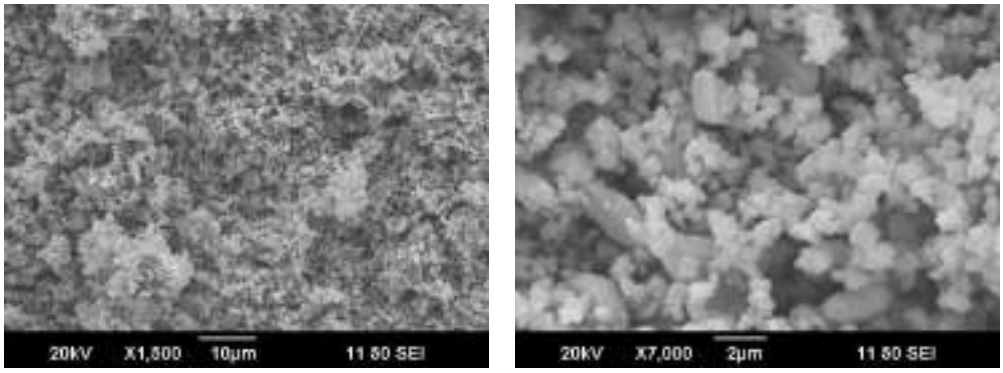

Figure 3: SEM images of $Cu_{0.75}Ni_{0.25}CrO_2$ samples with different magnification.

Ni^{2+}, intensity of all peaks decreased because of its low crystallinity. D H Ursu et.al also observed similar result[13]. Higher substituted samples shows more impurity peaks than lower substituted. A lower angle shift of the XRD peaks are due to difference in ionic radii of Cr^{3+} and Ni^{2+}. S Y Zheng et.al observed a considerable shift in the Ni doped $CuCrO_2$, for the peak (0 0 6) attributed to the difference in the ionic radius of $Cr^{3+}(0.63A°)$ and $Ni^{2+}(0.69A°)$[12]. $CuAlO_2$ also showed similar shift when doped by Mg^{2+}[14].

Figure 2 shows FTIR spectra of Ni substituted copper chromate. Two strong bands are observed at around 500 cm^{-1} and 700 cm^{-1} which corresponds to Cu-O stretching vibration and Cr-O stretching vibration respectively. Tokeer Ahmad et.al reported two similar characteristic bands near 536 and 743 cm^{-1} for the Cu-O and Cr-O stretching frequencies[15].

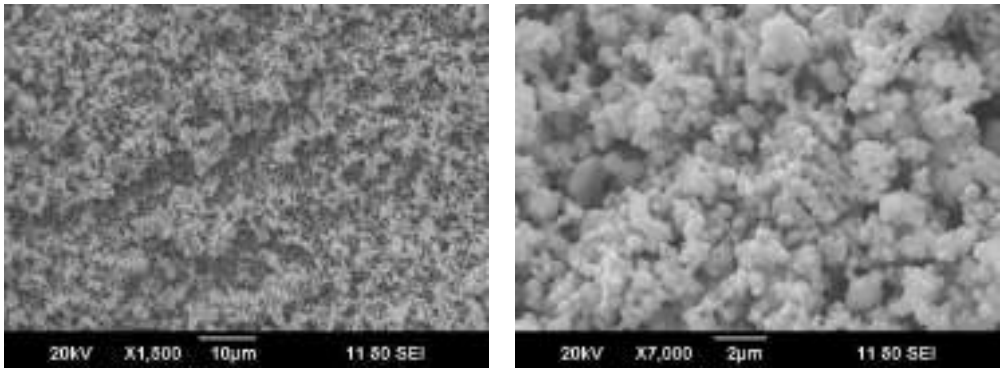

Figure 4: SEM images of $Cu_{0.5}Ni_{0.5}CrO_2$ samples with different magnification.

SEM micrographs of the samples at different magnifications are shown in figure 3 and 4. Nanocrystallinity of the agglomerated particles were confirmed.

Conclusion

Nickel substituted $CuCrO_2$ was prepared by a simple sol-gel method. Synthesized powder samples of $Cu_{1-x}Ni_xCrO_2$ were annealed and characterized. Influence of Ni substitution on structural and morphological properties of $CuCrO_2$ were studied. XRD studies showed $CuCrO_2$ as the main phase with some peaks of spinel crystalline phase. Due to difference in ionic radii of Cr^{3+} and Ni^{2+}, XRD peaks are slightly shifted towards lower diffraction angles which confirms the substitution of Ni. FTIR spectra of the samples also confirmed the formation of copper chromate. SEM images demonstrated the nanocrystalinity of the samples with agglomerated particles.

Acknowledgments

K. V. Shilna acknowledges the financial support obtained from KSCSTE, Govt. of Kerala under the scheme of PhD research fellowship.

References

[1] Satish Bolloju et.al, *Bull. Mater. Sci.*, **40**, 195-199, (2017).

[2] Amrute A P et.al., *J. Angew. Chem. Int. Ed.*, **52** 9772, (2013).

[3] Zhou S et.al., *Sensor Actuat. B*, **143**, 119, (2009).

[4] Kameoka S et.al., *Catal. Lett.*, **120** ,252, (2008).

[5] Meng Q et.al., *J. Sol–Gel Sci. Technol.*, **63**,1, (2012).

[6] Wiley A. Dunlap-Shohl et.al., *J. Mater. Chem.A*, 1-10, (2017).

[7] M. Ngo et.al., *RSC Adv.*, 1-20, (2016).

[8] Kawazoe et.al., *Nature*, **389**, 939, (1997).

[9] R. Nagarajan et.al., *J. Appl. Phys.*, **89**, 8022- 8025, (2001).

[10] M. Amami et.al., *Mater. Res. Bull.*, **46**, 1729–33, (2011).

[11] Y. F. Wang, Y. J. Gu, T. Wang, W. Z. Shi, *J. Sol-Gel Sci. Technol.*, **59**(2), 222(2011).

[12] Zheng S Y, Jiang G S, Su J R and Zhu C F, *Mater. Lett.*, **60**, 3871–3, (2006).

[13] Ursu D et.al., *J. Nanosci Nanotechnol*, **6**, 71–76, (2016).

[14] Jiang H F et al, *J. Alloys Compounds*, **509**, 1768–73, (2011).

[15] Tokeer Ahmad et.al., *RSC Adv.*, **7**, 27549–27557, (2017).

Fluctuation measure in pure gluon plasma using quasiparticle model

Simji P
Department of Physics, S.A.R.B.T.M Government College,Koyilandy,
Kozhikode, Kerala-673305

Abstract

The specific heat capacity which, the only fluctuation measure in pure gluon plasma and the associated quantity-the velocity of sound, have direct physical relevance for heavy ion collision experiments.We study the statistical mechanics and thermodynamics of pure gluon plasma using one of the phenomenological models of quark gluon plasma (QGP), the quasiparticle model (qQGP). Using this equation of state we calculate specific heat capacity and velocity of sound in pure gluon plasma and are compared with the available lattice results. We also predict the behaviour of these quantities in the large temperature range (upto $1000T_c$) in which studies have not been reported yet. Also this study provides a test for the suitability of this model being used as phenomenological models of QGP that are trying to explain the lattice data.

Introduction

The detailed knowledge of the QCD (quatum chromodynamics) equation of state is of crucial importance in various aspects such as the hydrodynamical description of heavy ion collision experiments, the evolution of early universe and the properties of compact stellar objects like neutron stars. Even though the perturbative calculation results are now available up to the order of $O(g^6)$ [1], it is inadequate for the calculation of QCD thermodynamic quantities in the temperature region accessible to the heavy ion collision experiments, because of the bad convergence of the expansion in the strong coupling constant. Consequently phenomenological models have been developed. But the most effective approach based on first principle calculation of the QCD properties is lattice QCD [2–4]. However we have to depend on the phenomenological models which allow for a more pictorial view on to the nature of QCD matter. In this article we derive the equation of state of pure gluon plasma by studying the statistical mechanics and thermodynamics using phenomenological model like quasiparticle model and then we go beyond the equation of state (EoS) and study the fluctuation measure in pure gauge plasma. The most useful way to study the fluctuations in a system created in heavy ion collision is the study of event-by-event fluctuations in which a given observable is measured on an event-by-event basis. Nowadays these event-by-event fluctuations of quantities have been of great interest as the signature of quark-hadron phase transition. As the quark gluon plasma (QGP) has only a transient existence in the heavy ion collision

experiment, we depend on different signatures for the formation of QGP as the probes for the plasma phase of QCD. So if an observable whose fluctuation survives the freeze out of fireball, that fluctuation can be used as a probe for the existence of QGP. In the case of pure gluon plasma, the specific heat capacity is the only fluctuation measure and evolution of this fluctuation is related to the value of another quantity called velocity of sound.

It is suggested that the specific heat capacity is directly related to the event-by- event temperature fluctuations [5] and transverse momentum (p_T) fluctuations [6] in the heavy ion collision experiment. These fluctuations can be measured in heavy ion collisions. On the other hand the measurement of these fluctuations give us an idea about the heat capacity. There are many attempts to measure this specific heat capacity in RHIC [7]. The specific heat capacity can be used to study the phase transitions and other thermodynamics of the system.

The velocity of sound determine the flow properties in the heavy ion collisions [8, 9]. It controls the expansion rate of fireball in the heavy ion reaction and are important in the hydrodynamic description of QGP. One of the signature of QGP formation in heavy ion collision experiment, the elliptical flow, is found to be sensitive [8–10] to the value of sound velocity.

Quasiparticle model is the one of the successful model widely used for studying the equation of state of QGP in literature. Vareties of the many quasiparticle models [11–19], we use two widely studied quasiparticle models. One with reformulated statistical mechanics which has more than three phenomenological parameters and gives reasonably good fit to the lattice result (QPM I) [12, 13]. Second quasiparticle model is a single parameter model that need no reformulation of statistical mechanics, but gives good fit to the lattice results (QPM II) [14,15]. In [20] we have compared QPM I and QPM II in the context of QED plasma and found that they are equally good in explaining the statistical mechanics and thermodynamics of ultra-relativstic QED plasma. From [21] also we found that these models are good in explaining lattice result [26] of pure gluon plasma for a large temperature range. Here we use both of these models for calculating the statistical mechanics and thermodynamics of pure gluon plasma and further we study the behaviour of specific heat capacity (C v) and velocity of sound (C s) of pure gluon plasma with QPM I and QPM II up to 1000T c . The advantage of this fluctuation study is that it provide a further test for the suitability of the models being used as phenomenological models.

Theory

In the quasiparticle model, the effect of interaction leads to thermal excitation of quasiparticles with thermal mass which depends up on the temperature and strong coupling constant. The simple dispersion relation for energy ε_k and momentum k of the quasiparticle is

$$\varepsilon_k = \sqrt{k^2 + m^2 T} \tag{1}$$

$m(T)$ is the temperature dependent mass or thermal mass of the particle. There are different forms of thermal masses used in different quasiparticle models. The effective gluon mass taken in QPM I and QPM II are the two different approximate limits of an exact dispersion relation given in [15, 29]. In the weak

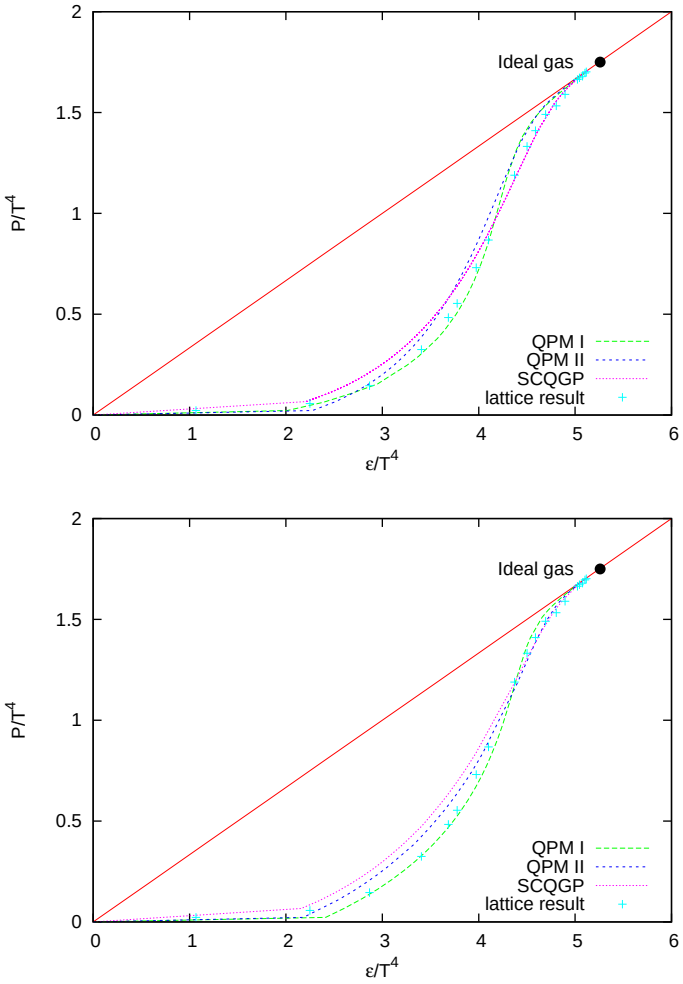

Figure 1: The equation of state of QCD matter from three models using one-loop and two-loop order running coupling constants. The diagonal line denotes EoS of theories with conformal symmetry. The circle on the diagonal denotes the ideal gluon gas. Lattice result is also shown for comparison.

coupling limit it can be approximated as $\varepsilon_k^2 = \alpha k^2 + \beta\omega_p^2$ with $\alpha = 1(6/5)$ and $\beta = 3/2(1)$ at large (small) momenta. ω_p is the plasma frequency

which is given by $\omega_p^2 = \frac{g^2(T)T^2}{3}$, obtained from perturbative QCD calculations. QPM I uses the approximaton in which $\beta = 3/2$, so that $m^2(T) = \frac{3}{2}\omega_p^2$ [13]. Thus the thermal mass of gluon and the coupling constant utilized in this model [13] are

$$m^2(T) = \frac{1}{2}g^2(T)T^2 \tag{2}$$

and

$$g^2(T) = \frac{48\pi^2}{11N_c ln(\lambda\frac{T}{T_c} + \frac{T_s}{T_c})^2} \tag{3}$$

with T_s/T_c as the phenomenological regularization and T_c/λ represents the usual regularization scale parameter Λ . In QPM II the author argues that the above approximation for thermal mass is valid only for the weak coupling limit but QGP with temperature near T_c is not a weakly coupled system. So as a phenomenological model and motivated from similar work on electrodynamic plasma [22, 23], in QPM II gluon mass approximation used is $m^2(T) = \omega_p^2$ [14, 15]. So the effective mass or thermal mass of gluon used in QPM II is

$$m^2(T) = \frac{g^2(T)T^2}{3} \tag{4}$$

and here $g^2(T)$ is related to the two-loop order running coupling constant [14, 15] as

$$g^2(T) = 4\pi\alpha_s(T) = \frac{24\pi^2}{(33-2n_f) - ln(T/\Lambda_T)}(1 - \frac{3(153-19n_f)^2}{(33-2n_f)}\frac{ln(2ln(T/\Lambda_T))}{ln(T/\Lambda_T)}) \tag{5}$$

where Λ_T is a parameter related to scale parameter. But here in our work we apply one-loop and two-loop order coupling constants in both models. As QPM I and QPM II are based on different formulation, the definitions of thermal mass used in these models are such that they give the best fit to the lattice data.

In the formulation of the first thermodynamically consistent quasiparticle model, which has reformulated sta- tistical mechanics [12, 13] (QPM I), one starts from pressure,

$$p(T) = \frac{d_f}{6\pi^2}\int dk \frac{k^4}{\sqrt{k^2+m^2(T)}}\frac{1}{e^{\frac{1}{T}\sqrt{k^2+m^2(T)}} - 1} - B(T) \tag{6}$$

energy density is

$$\varepsilon(T) = \frac{d_f}{2\pi^2}\int dk k^2 \sqrt{k^2+m^2(T)}\frac{1}{e^{\frac{1}{T}\sqrt{k^2+m^2(T)}} - 1} + B(T) \tag{7}$$

where d_f is the gluon degeneracy factor. These equations involves a temperature dependent extra function B(T) inorder to keep the system thermodynamically consistent

$$B(T) = B_0 - \frac{d_f}{4\pi^2}\int dT \frac{dm^2(T)}{dT}\int \frac{k^4}{\sqrt{k^2+m^2(T)}}\frac{1}{e^{\frac{1}{T}\sqrt{k^2+m^2(T)}} - 1} \tag{8}$$

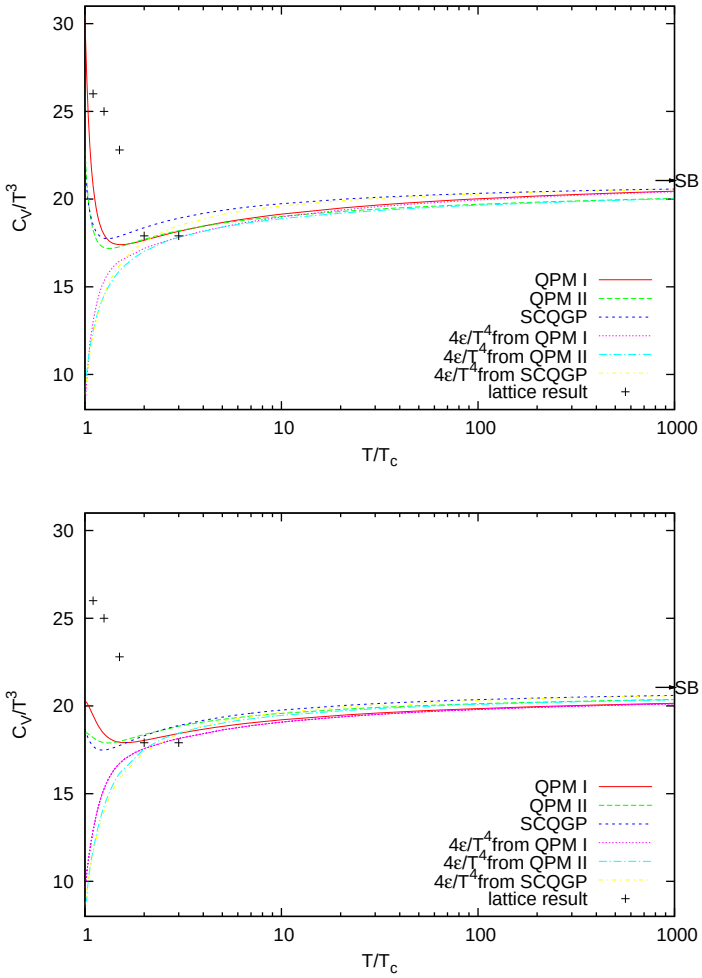

Figure 2: Three model result for C_v/T^3 using one-loop (a) and two-loop (b)order running coupling constants. $4\varepsilon/T^3$ is also plotted for comparison

[13] where B_0 is the integration constant, i.e., the value of B(T) at $T = T_0$ and T_0 is some reference temperature. According to reference [14, 15] the author pointed out the reason for the thermodynamic inconsistency of the quasiparticle description of Peshier et al. [11] If the particle mass is temperature dependent, the relation between the pressure and grand partition function may not be true. Hence in QPM II we start from the definition of average energy in the grand canonical ensemble,

$$\varepsilon = \frac{1}{V}\Sigma\frac{\varepsilon_k e^{-\frac{1}{T}\varepsilon_k}}{1 - e^{-\frac{1}{T}\varepsilon_k}} \tag{9}$$

and we get,

$$\varepsilon(T) = \frac{d_f}{2\pi^2}T^4\Sigma\frac{1}{l^4}[3(\frac{ml}{T})^2K_2(\frac{ml}{T}) + (\frac{ml}{T})^3K_1(\frac{ml}{T})] \tag{10}$$

where K_1 and K_2 are modified Bessel functions . The pressure can be derived from the thermodynamic relation

$$\varepsilon(T) = T\frac{\partial P}{\partial T} - P \tag{11}$$

on integration, where the value of the integration constant is being fixed from lattice data at transition temperature. Thus this model is statistically and thermodynamically consistent even with out B(T).

Specific heat and velocity of sound

For a relativistic gas, the particles are created and destroyed and hence the only fluctuation measure in the absence of chemical potential, is the specific heat capacity at constant volume. Also in the absence of chemical potential the quantity like compressibility is not defined. But the quantity velocity of sound is well defined. Once we know the energy density and pressure, we can easily evaluate specific heat capacity and velocity of sound. These two quantities are defined as The specific heat at constant volume C_v is

$$C_v = \frac{\partial\varepsilon}{\partial\varepsilon}|_v \tag{12}$$

and velocity of sound squared C_s^2 is

$$\begin{aligned} C_s^2 &= \frac{\partial p}{\partial\varepsilon}|_s \\ &= \frac{\partial p}{\partial T}|_v(\frac{\partial\varepsilon}{\partial T}|_v) - 1 \\ &= \frac{s/T^3}{C_v/T^3} \end{aligned} \tag{13}$$

Results and Discussion

In figure 1 we plotted the equation of state P/T^4 against ε/T^4 of pure gluon plasma for a large temperature range $(1 - 1000)T_c$ using quasiparticle models.

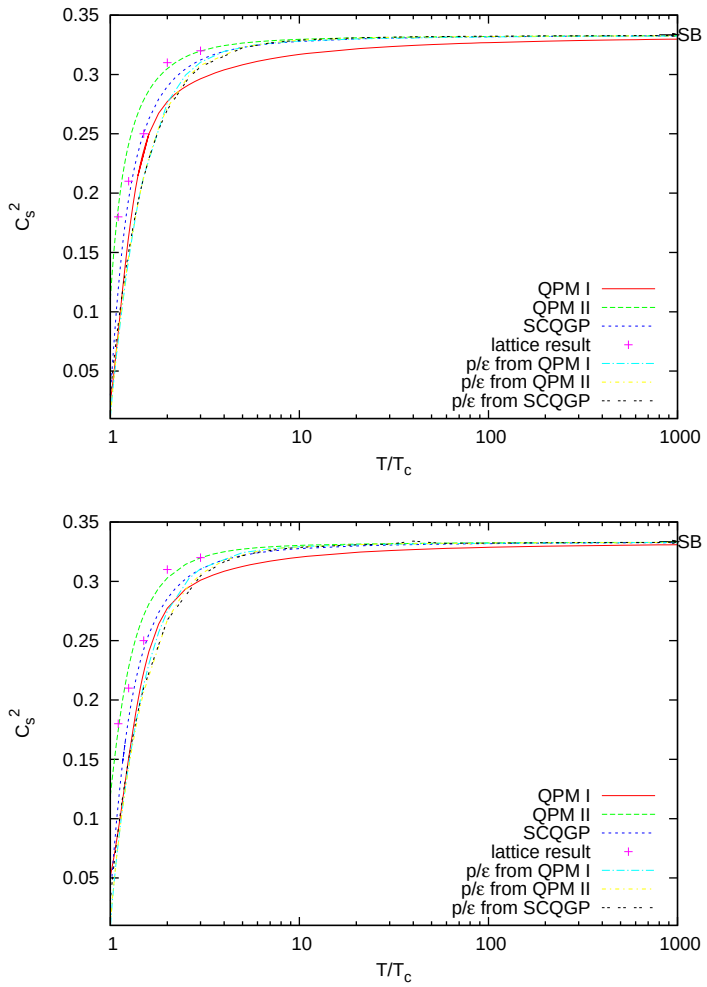

Figure 3: Three model result for C_s^2 using one-loop (a) and two-loop (b) order running coupling constants. P/ε is also plotted for comparison

The lattice results from [26] are also plotted for comparison. We also compare the result of another phenomenological model of QGP, the strongly coupled quark gluon plasma model (SCQGP model) [21, 24, 25] which also trying to explain the non-ideal behaviour of QGP, for comparison. The diagonal line represents the possible equation of state for theories with conformal symmetry where $\varepsilon = 3p$. The ideal gluon gas with $N_c = 3$ is represented as a circle on the diagonal and whose equation of state is temperature independent. From the figure it is to be noted that the pure gauge QCD is close to the conformal line in the high temperature region and deviate very much in the low temperature region especially near the transition temperature, T_c . Thus become more and more non ideal as temperature decreases to T_c and this may be due to the formation of massive glueballs in gluon plasma near T_c . Three model calculation results and lattice data shows same behaviour. Also even at $1000T_c$, the equation of state of pure glue plasma does not attain the ideal gluon gas value which means that in the gluon plasma the interaction exist even at these high temperatures and hence it is non-ideal.

In figure 4.2, three model results for C_v/T^3 is plotted and compared with the lattice results [27,28] and the value of $4\varepsilon/T^4$, at which the C_v/T^3 coincide for a conformal gas. The available lattice result is up to $3T_c$ and is clear from the figure that C_v/T_3 peaks at T_c and decreases sharply for a short range, then increases slowly and approaches the corresponding Stefan-Boltzmann limit for high temperatures. In the low temperature region very close to $T = T_c$ the lattice calculation results and our phenomenological calculation results show some discrepancy and which may be because there is no consideration for confinement and strong coupling effect close to T_c in our models. But as the temperature reaches 2 to 3 times T_c , the lattice results and our model calculation results are in good agreement. Also the value of C_v/T^3 is almost consistent with the predictions of the conformal theories that $C_v/T^3 = 4\varepsilon/T^4$ at high temperatures but not as perfectly as given in ref. [28]. Similar result was obtained in [29] even though they included quarks in their calculations. But closer to T c there is a mismatch. The sharp peak of C_v/T^3 at T c shows that the pure gauge theory has a first order phase transition and also it is clear that one has to supply a large amount of heat to increase the temperature across T_c to liberate gluon degrees of freedom. One more thing is that even at temperature of $1000T_c$, C_v/T^3 and $4\varepsilon/T^4$ show significant deviation from the Stefan-Boltzmann limit. It is also clear that all three models shows same behaviour. In figure 4.3 we have plotted both the value of velocity of sound and the ratio p/ε as a function of temperature. For temperatures of the order 2.5-3 T_c and above p/ε matches with C_s^2 . But below 2.5 T_c , C_s^2 is always greater than p/ε. Moreover all the three models have similar behaviour with sharp rise near T_c , then flattened and reaches a value very close to the Stefan-Boltzmann limit of $C_s^2(1/3)$ much faster.

Conclusion

In this paper we have studied the behaviour of specific heat capacity, which is the only fluctuation measure in pure gluon plasma and associated quantity, the velocity of sound which is an important input in the hydrodynamical study, using quasiparticle models and strongly coupled quark gluon plasma model. We

also tried to predict the behaviour of these quantities for large temperature range (up to 1000 T_c) because the available lattice calculation for these quantities are up to 3 T_c for specific heat [28] and up to 5 T_c for velocity of sound and. It is found that C_v/T^3 calculated using our phenomenological models shows almost same behaviour as lattice result for temperature close to T_c and in good agreement at around 2 T_c and above. The peak of C_v/T^3 at T_c suggests that the transition of pure gluon plasma is a first order one. Our result for the quantity C_s is also consistent with the lattice calculations. Based on our model calculation results, it can be argued that the gluon plasma phase is not far from the conformal symmetric limit at high temperature, but deviates sharply near T_c . Also even at a temperature of 1000 T_c , equation of state of gluon plasma does not coincide with that of pure ideal gluon plasma and hence it is non ideal. Since our model calculation results are consistent with the lattice calculation data, it gives us confidence in using these models as phenomenological models for gluon plasma for large range of temperature.

References

[1] K. Kajantie, M. Laine, K. Rummukainen and Y. Schroder, Phys. Rev. D 67, 105008 (2003) [arXiv:hep- ph/0211321]

[2] G. Boyd, J. Engels, F. Karsch, E. Laermann, C. Legeland, M. Lutgemeier, B. Petersson, *Phys. Rev. Lett.*, 75 (1995); *Nucl. Phys. B*, 469, 419 (1996).

[3] F. Karsch, *Nucl. Phys. A*, 698, 199 (2002); F. Karsch, E. Laermann, A. Peikert, *Phys. Lett. B*, 478, 447(2000).

[4] E. Laermann, O. Philipsen, *Ann. Rev. Nucl. Part. Sci.*, 53, 163 (2003).

[5] L. Stodolsky, *Phys. Rev. Lett.*, 75, 1044 (1995).

[6] R. Korus, S. Mrowczynski, M. Rybczynski and Z. Wlodarczyk, *Phys. Rev. C*, 64, 054908 (2001).

[7] M. J. Tannenbaum [PHENIX Collaboration], nucl-ex/0512004.

[8] H. Sorge, *Phys. Rev. Lett.*, 82, 2048 (1999).

[9] P. F. Kolb, J. Sollfrank and U. Heinz, *Phys. Lett. B*, 459 (1999) 667; P. F. Kolb, J. Sollfrank, P. V. Ruuskanen and U. Heinz, *Nucl. Phys. A*, 661, 349 (1999).

[10] D. Teaney, J. Lauret and E. V. Shuryak, *Phys. Rev. Lett.*, 86, 4783 (2001); nucl-th/0110037.

[11] M.I. Gorenstein, S.N. Yang, *Phys. Rev. D*, 52, 5206 (1995).

[12] A. Peshier, B. Kampfer, O.P. Pavlenko, G. Soff, *Phys. Lett. B*, 337, 235 (1994).

[13] A. Peshier, B. Kampfer, O.P. Pavlenko, G. Soff, *Phys. Rev.D*, 54, 2399 (1996).

[14] V.M. Bannur, *Eur. Phys. J. C*, 50, 629 (2007); *Phys. Lett. B*, 647, 271 (2007); *JHEP*, 09, 046 (2007)

[15] V.M. Bannur, *Phys. Rev.C*, 75, 044905 (2007).

[16] P. Levai and U. Heinz, *Phys. Rev. C*, 57, 1879 (1998).

[17] R. A. Schneider and W. Weise, ibid. 64,055201 (2001).

[18] D. H. Rischke, *Prog. Part. Nucl. Phys.*, 52, 197 (2004).

[19] F.G. Gardim and F.M. Steffens, *Nucl. Phys. A*, 797, 50 (2007).

[20] Simji. P and Vishnu M. Bannur, *Eur. Phys. J. D*, 66, 244 (2012).

[21] Simji, P and Vishnu M. Bannur, *Int. J. Mod. Phys. A*, 28, 1350121 (2013).

[22] M. V. Medvedev, *Phys. Rev. E*, 59, R4766 (1999).

[23] V. M. Bannur, *Phys. Rev. E*, 73, 067401 (2006).

[24] V.M. Bannur, *Eur. Phys. J. C*, 11, 169 (1999).

[25] V.M. Bannur, *J. Phys. G: Nucl. Part. Phys.*, 32, 993.

[26] Sz. Borsanyi, G. Endrodi, Z. Fodor, S.D. Katz, K.K. Szabo, arXiv:1204.6184 [hep-lat].

[27] R. V. Gavai, S. Gupta and S. Mukherjee, *Phys. Rev. D*, 71, 074013 (2005).

[28] R. V. Gavai, S. Gupta and S. Mukherjee, *PoS LAT2005*„ 173 (2006); hep-lat/0506015.

[29] Sanjay K. Ghosh, Tamal K. Mukherjee, Sibaji Raha, *Mod.Phys.Lett.A*, 21:2067-2077(2006).

AGN signatures of the LSB galaxy UGC 2936

M. Honey[1], M. Das[2]
[1]S.A.R.B.T.M Government College Koyilandy, Kozhikode 673307, Kerala, India
[2]Indian Institute of Astrophysics, Bangalore 560034, Karnataka, India

Abstract

We present a study of the signatures of Active Galactic Nuclei (AGN) activity in the Low Surface Brightness (LSB) galaxy UGC 2936. AGN are the extremely luminous central regions of galaxies, that result from the accretion of mass onto a supermassive Black hole. LSB galaxies have optically dim disks and their masses are dominated by their dark matter content. These galaxies are generally slowly evolving systems and have low star formation rates. In this study , we examined the optical spectrum of the LSB galaxy UGC 2936 which was observed using the 2m Himalayan Chandra Telescope in Hanle, India. Our aim was to study the AGN characteristic emission lines and its position in the BPT diagram, in order to classify whether UGC 2936 belongs to star forming class or AGN class. It is found that the UGC 2936 is hosting an AGN.

Introduction

Active Galactic Nuclei (AGN) are the extremely luminous central regions of galaxies. The galaxies that host AGN are called active galaxies. The production of energy in AGN is due to the accretion of mass onto a central supermassive black hole from the surrounding hot accretion disk. As gas is accreted, energy is released. This energy radiated over all wavelength bands of the electromagnetic spectrum. In normal High Surface Brightness (HSB) galaxies approximately 43% are active galaxies (Ho, Filippenko & Sargent 1997; She, Ho & Feng 2017).

Low Surface Brightness (LSB) galaxies are optically dim galaxies that are dominated by their dark matter content. These galaxies are generally slowly evolving systems and have low star formation rates. There are a few studies on the nulear activity in LSB galaxies (Schombert, 1998; Das et al., 2007, 2009; Naik et al., 2010; Galaz et al., 2011; Ramya, Prabhu & Das, 2011; Mishra et al., 2015; Subramanian et al., 2016). In LSB galaxies the number of active galaxies is less compared to that of HSB galaxies. This happens due to the lack of strong instabilities that drive the gas toward the

central regions. The presence of massive dark matter content supress the formation of structures like bars and spiral arms (Mayer & Wadsley, 2004; Ghosh & Jog, 2014; Honey et al., 2016)

In this study, we searched for the signatures of AGN activity in the LSB galaxy UGC 2936 using long slit optical spectroscopy. The observation and reduction details are described in the next Section. The analysis of the spectrum and the position of UGC 2936 on BPT diagram is discussed in Analysis and Results.

Data

The optical long slit spectrum of UGC 2936 was observed with the 2m Himalayan Chandra Telescope (HCT). The telescope control was done from the Centre For Research & Education in Science Technology (CREST) campus, Bangalore. The slit used was 11' × 1.92. The grism # 7 was used that has a dispersion of 1.46Å and a wavelength coverage of 3700-7200Å . The details of the galaxy and observation is shown in Table 2. The observations were carried out with a slit position along the bar of the galaxy and the nuclear region of the galaxy was well covered with the slit. The wavelength calibration were done with the ferrous argon (FeAr) arc lamp and the flux was calibrated using the standard stars (Oke, 1990) which were near the target galaxy.

The data reduction was done with the software package IRAF. The preprocessing steps including trimming and bias subtraction were carried out using the tasks IMCOPY, ZEROCOBIME and IMARITH. The one dimensional spectrum was extracted, using the APALL task that involves the steps of defining the aperture, extraction and tracing of the spectrum along the wavelength dispersion axis. The resultant spectrum includes the error spectrum. The calibration lamp spectrum also extracted with reference to the galactic spectrum. The task IDENTIFY was used to make the pixel to wavelength mapping. The wavelength calibrated spectrum was flux calibrated using the standard star spectrum observed on the same night using task called STANDARD. The resolution of the spectrum was determined with the sky line at 5577Å . The spectral resolution was about $\sim$ 8.5Å at 5577Å for grism # 7. The flux calibrated spectrum was corrected for redshift. The reddening correction for the galaxy was also done. The error spectrum was seperated from the galacic spectrum, using the task SCOPY.

Table 1: The parameters of LSB galaxy UGC 2936. The first column represent the galaxy name, the right acsension and decliantion of the galaxy is shown in second and third column. The redshift is shown in fourth column. The fifth, sixth and seventh columns shows the minor axis, major axis and morphology in NASA Extragalactic Database (NED) respectively.

Galaxy name	RA J2000.0	Dec J2000.0	Redshift	Major Diameter(')	Minor Diameter(')	Morphology (NED)
UGC 2936	04h02m48.19s	+01d57m57.7s	0.012719	2.5	0.7	SB(s)d Sy2

Analysis

1 Decomposition of galactic spectrum

The nuclear spectrum from the galactic centre contains contributions from the stellar continuum, emission from gaseous nebula and the power law from the AGN. We used the single stellar population (SSP) template spetra from MILES models. The template spectra of the same resolution were taken to fit the galactic spectra. All template spectra used for fitting were trimmed for the same wave length range as that of the galactic spectrum with IDL programmes. The fitting was done with penalized pixel fitting (pPXF) code (Cappellari & Emsellem, 2004). The code first masks the emission lines in order to obtain the stellar continuum. Since the pixel space is used for fitting, it is easier to mask the emission lines. The code needs the galactic spectrum and error spectrum as inputs. After masking, the stellar continuum was fitted with the weighted sum of template spectra and gauss-hermite polynomials to obtain the stellar continuum. Initial estimates were provided for fitting. The Monte Carlo optimization technique used to determine the minimum χ^2 and best matching steallar continnum. The best fitting stellar continuum was subtracted from the galactic spectrum to obtain the emission line spectrum. The galactic decomposition is shown in Figure 1

2 Fitting of emission lines

The seperated emission line spectrum was examined carefully. The earlier studies showed that emission from the Broad Line Region (BLR) clouds appear as broad emission lines in the emission line sepctrum (Peterson, 1997,

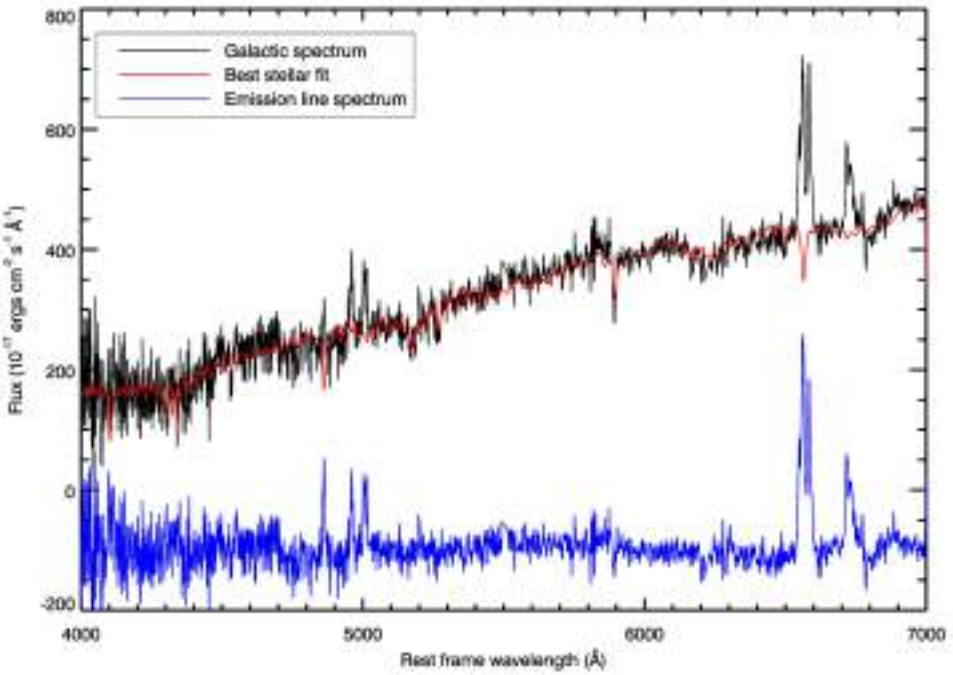

Figure 1: The spectral decomposition of UGC 2936 is shown here.

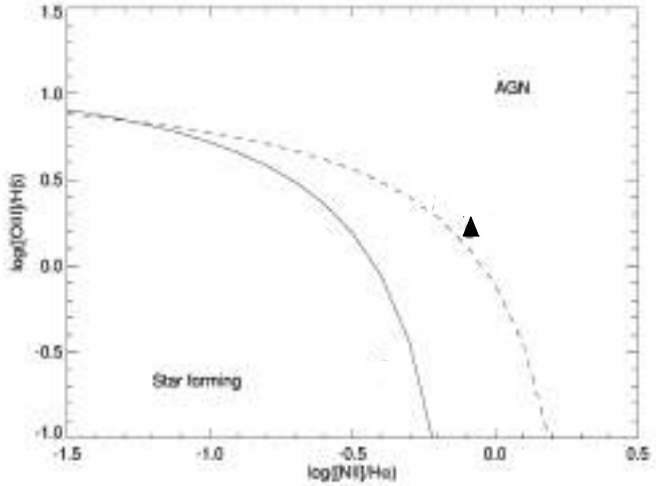

Figure 2: The BPT diagram of UGC 2936 with [OIII]/Hβ versus [NII]/Hα is shown. It clearly shows the galaxy is fall in AGN category.

Table 2: The observation details of UGC 2936

galaxy	exposure time(s)	date of observation
UGC 2936	3600	2014-01-24

2006). The AGN are generally characterized by the presence of emission lines like Hβ (4862Å), Hα (6563Å), [OIII] line (5007Å), [NII] lines (6548Å & 6583Å) and [SII] lines (6717Å & 6731Å). All these emission lines were individually fitted withMPFITFUN. The code GAUSS1 was used in MPFITFUN . The profile of the individual emission lines for each of these emission lines are different. The emission line fiting was done in a method similar to that used in Subramanian et al. (2016). For lines Hβ, Hα can have two components, one broad component and one narrow line component. Each of these components were seperated and their fluxes were calculated. The models used for these fittings were defined by multiple (two or more) gaussian functions. For example the Hα-[NII] lines region, the model used has four gausian functions - three for narrow line components (one for Hα and two for [NII] lines) and one for broad line component. Simillarly the [SII] regions were fitted with two equal width gaussian functions.

3 AGN calssification and BPT diagram

There are different types of AGN. Like the AGN, the star forming galaxies also show some characteristic emission lines. The emission mechanism can be found out by examining the strength of characteristic atomic emission lines. Based on the emssion line fluxes, J. A. Baldwin, M. M. Phillips and Roberto Terlevich proposed a method to classify the galaxies and the method is called the BPT diagram. There are two diagrams with [OIII]/Hβ versus [NII]/Hα and [OIII]/Hβ versus [SII]/Hα. From Kewley et al. (2001),Kauffmann et al. (2003) and Kewley et al. (2006) we have taken the demarcation lines. The BPT diagram with [OIII]/Hβ versus [NII]/Hα is shown in Figure 2. The figure shows that UGC 2936 falls in the AGN category.

Conclusions

Our optical study of the LSB galaxy UGC 2936 shows that the galaxy has emission lines characteristic of AGN activity. The BPT diagram is the main tool for the emperical classification. The ratio of line fluxes shows that the sample galaxy is hosting an AGN. This supports the earlier studies that the LSB galaxies can host AGN.

Acknowledgments

The observations were done with HCT at the Indian Optical Observatory (IAO) at Hanle. We thank the staff of IAO, Hanle and CREST, Hosakote, that made these obervations possible. The facilities at IAO and CREST are operated by the Indian Institute of Astrophysics, Bangalore. This research has made use of the NASA/IPAC Extragalactic Database (NED), which is operated by the Jet Propulsion Laboratory, California Institute of Technology, under contract with the National Aeronautics and Space Administration.

References

Cappellari M., Emsellem E., 2004, *Publications of the Astronomical Society of the Pacific*, 116, 138

Das M., Kantharia N., Ramya S., Prabhu T. P., McGaugh S. S., Vogel S. N., 2007, *Monthly Notices of the Royal Astronomical Society*, 379, 11

Das M., Reynolds C. S., Vogel S. N., McGaugh S. S., Kantharia N. G., 2009, *The Astrophysical Journal*, 693, 1300

Galaz G., Herrera-Camus R., Garcia-Lambas D., Padilla N., 2011, *The Astrophysical Journal*, 728, 74

Ghosh S., Jog C. J., 2014, *Monthly Notices of the Royal Astronomical Society*, 439, 929

Ho L. C., Filippenko A. V., Sargent W. L. W., 1997, *The Astrophysical Journal*, 487, 568

Honey M., Das M., Ninan J. P., Manoj P., 2016, *Monthly Notices of the Royal Astronomical Society*, 462, 2099

Kauffmann G. et al., 2003, *Monthly Notices of the Royal Astronomical Society*, 346, 1055

Kewley L. J., Dopita M. A., Sutherland R. S., Heisler C. A., Trevena J., 2001, *The Astrophysical Journal*, 556, 121

Kewley L. J., Groves B., Kauffmann G., Heckman T., 2006, *Monthly Notices of the Royal Astronomical Society*, 372, 961

Mayer L., Wadsley J., 2004, *Monthly Notices of the Royal Astronomical Society*, 347, 277

Mishra A., Kantharia N. G., Das M., Srivastava D. C., Vogel S. N., 2015, *Monthly Notices of the Royal Astronomical Society*, 447, 3649

Naik S., Das M., Jain C., Paul B., 2010, *Monthly Notices of the Royal Astronomical Society*, 404, 2056

Oke J. B., 1990, *The Astronomical Journal*, 99, 1621

Peterson B. M., 1997, An Introduction to Active Galactic Nuclei

Peterson B. M., 2006, in Lecture Notes in Physics, Berlin Springer Verlag, Vol. 693, Physics of Active Galactic Nuclei at all Scales, Alloin D., ed., p. 77

Ramya S., Prabhu T. P., Das M., 2011, *Monthly Notices of the Royal Astronomical Society*, 418, 789

Schombert J., 1998, *The Astronomical Journal*, 116, 1650

She R., Ho L. C., Feng H., 2017, *The Astrophysical Journal*, 842, 131

Subramanian S., Ramya S., Das M., George K., Sivarani T., Prabhu T. P., 2016, *Monthly Notices of the Royal Astronomical Society*, 455, 3148

McGaugh, & Vogel]das.etal.2007 Das M., Kantharia N., Ramya S., Prabhu T. P., McGaugh S. S., Vogel S. N., 2007, *Monthly Notices of the Royal Astronomical Society*, 379, 11

Ground state energy and Binding energy of an exciton in a GaAs quantum dot in the presence of an external magnetic field

Luhluh Jahan K
School of Physics, University of Hyderabad, Hyderabad - 500046.

Abstract

The problem of an exciton trapped in a three dimensional Gaussian quantum dot is studied in the presence of an external magnetic field. A variational method is employed to obtain the ground state energy and the binding energy of the exciton as a function of the quantum dot size, the confinement strength and the magnetic field.

Introduction

A quantum dot (QD) can be considered to be a nanocrystal or a giant artificial atom that is small enough to exhibit quantum mechanical properties[1]. QD's are interesting because of their potential applications in opto-electronic devices like quantum dot lasers[2], ultrafast systems like quantum computers and in microelectronic devices like single electron transistors[3]. It has been observed that quantum confinement dramatically changes the optical and electronic properties of QD's. In semiconductor QD's, excitons which are excitations comprising bound electron-hole pairs play a central role in optoelectronic devices such as photovoltaic cells and light emitting diodes[4, 5, 6, 7, 8, 9]. Early experiments [10,11] together with the generalized Kohn theorem [12,13] indicated that the confining potential in a QD is parabolic and this led to a host of theoretical investigations to study the electronic properties of QD's [14-21]. Several authors have also used the parabolic potential model to explore the properties of excitons in QD's [22-26].

But, some recent experiments suggest that the confining potential in a QD is anharmonic and has a finite depth. Adamowsky et al [27] have proposed an attractive Gaussian potential which seem to mimic the actual confining potential better. The Gaussian potential has already been used by several authors as the model for confinement to study the electronic properties of a QD [28-46]. In the present work we shall calculate the GS energy and binding energy (BE) of an exciton in a spherical Gaussian quantum dot

in the presence of an external magnetic field as a function of quantum dot radius, magnetic field and the potential strength using a variational method.

Model

The Hamiltonian of an exciton in a Gaussian QD in the presence of a magnetic field B can be written as

$$H = \sum_{i=e,h} \left[\frac{1}{2m_i^*} \left(p_i + \frac{q_i}{c} A_i \right)^2 + V(r_i) \right] - \frac{e^2}{\varepsilon |r_e - r_h|}, \tag{1}$$

where $i = e$ represents an electron and $i = h$ a hole, q_e is the electronic charge and q_h is the hole charge., $r_i = r_e\,(r_h)$ refers to the position vector of the electron (hole), $p_i = p_e\,(p_h)$ is the corresponding momentum operator, $m_i^* = m_e^*\,(m_h^*)$ denotes the effective mass of the electron (hole), $A_i = A_e\,(A_h)$ is the vector potential for the electron (hole) corresponding to the magnetic field B which has been applied in the z direction, $V(r_i)$ is the confining potential of the quantum dot and ε is the dielectric constant of the material. The effective Hamiltonian can be written in the symmetric gauge as

$$\begin{aligned} H = \sum_{i=e,h} \left[-\frac{\hbar^2}{2m_i^*} \nabla_i^2 - V_0 e^{-\frac{r_i^2}{2R^2}} + \frac{1}{8} m_i^* \omega_{ci}^2 r_i^2 \right] \\ + \frac{1}{2} \left(\omega_{ce} L_{ze} - \omega_{ch} L_{zh} \right) - \frac{e^2}{\varepsilon |r_e - r_h|} \end{aligned} \tag{2}$$

where V_0 and R are respectively the depth and range of the single particle confinement potential in the QD.

Formulation

We can rewrite the Hamiltonian (2) as

$$H = H_0 + H_1 \tag{3}$$

where

$$\begin{aligned} H_0 = \sum_{i=e,h} \left[-\frac{\hbar^2}{2m_i^*} \nabla_i^2 + \frac{1}{2} m_i^* \omega_i^2 r_i^2 \right] - 2V_0 \\ + \frac{1}{2} \left(\omega_{ce} L_{ze} - \omega_{ch} L_{zh} \right) - \frac{e^2}{\varepsilon |r_e - r_h|} \end{aligned} \tag{4}$$

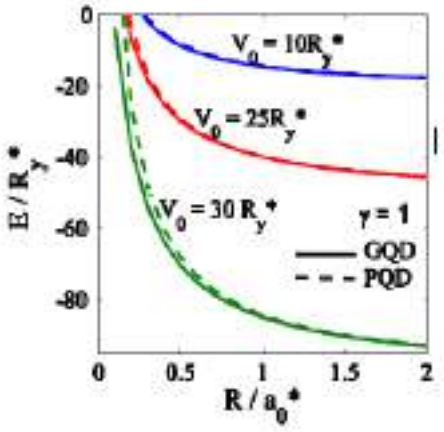

Figure 1: GS energy of an exciton in a 3D GaAs QD with Gaussian confinement as a function of the effective QD size (R) in the presence of a magnetic field for three values of the potential depth.

$$H_1 = -\lambda \sum_{i=e,h} \left[\frac{1}{2} m_i^* \omega_{i0}^2 r_i^2 + V_0 \left(e^{-\frac{r_i^2}{2R^2}} - 1 \right) \right] \tag{5}$$

where

$$\omega_i^2 = \omega_{i0}^2 + \frac{\omega_{ci}^2}{4} \quad ; \qquad \omega_{i0}^2 = \frac{V_0}{m_i^* R^2} \tag{6}$$

and $\lambda = 0$ for parabolic potential model and $\lambda = 1$ for Gaussian potential model. We are interested in the GS of the system and the L_z term does not make any contribution. We assume that the sole effect of H_i is to renormalize the frequency ω_i and so we treat H_i at the mean field level. More specifically we write H_1 as

$$\begin{aligned} H_1 =& \lambda \sum_{i=e,h} \left[\frac{V_0}{\langle r_i^2 \rangle} - \frac{1}{2} m_i^* \omega_{0i}^2 - \frac{V_0 \langle e^{-r_i^2/2R^2} \rangle}{\langle r_i^2 \rangle} \right] r_i^2 \\ =& \lambda \sum_{i=e,h} \omega_i^2 r_i^2 \end{aligned} \tag{7}$$

where $\langle r_i^2 \rangle$ is the expectation value of r_i^2 with respect to the GS wave function of the harmonic oscillator of frequency $\widetilde{\omega}_i$ [23]. Since $\langle r_e^2 \rangle = \langle r_h^2 \rangle$ and $\langle e^{-r_e^2/2R^2} \rangle = \langle e^{-r_h^2/2R^2} \rangle$, we can write $\widetilde{\omega}_e^2 + 2\,(\lambda/m_e^*)\,\omega_e^2 = \widetilde{\omega}_h^2 + 2\,(\lambda/m_h^*)\,\omega_h^2 \equiv \omega^2$. The Gaussian potential problem thus reduces to an effective parabolic potential problem described by the Hamiltonian,

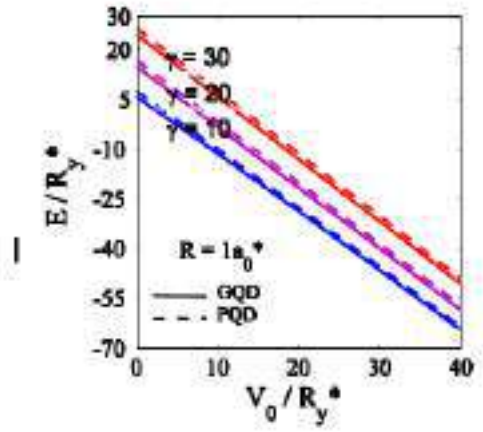

Figure 2: GS energy of an exciton in a 3D QD as a function of the confinement potential depth for three values of the magnetic field.

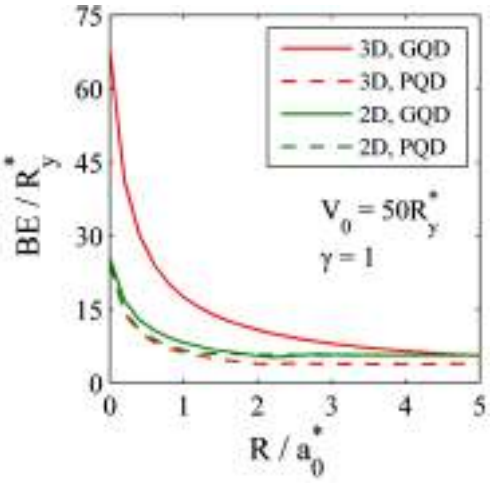

Figure 3: BE of an exciton in PQD and GQD as a function of the QD size in 2D and in 3D.

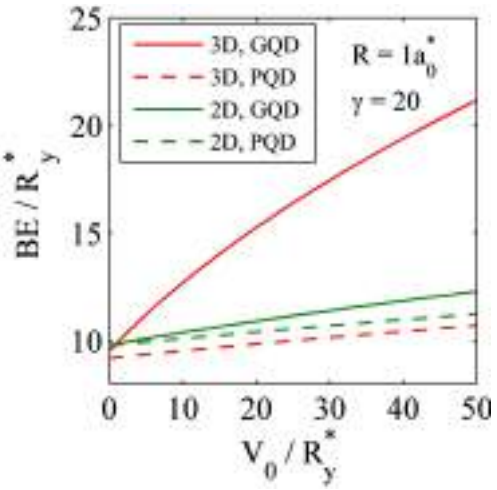

Figure 4: BE of an exciton in PQD and GQD as a function of the depth of the confining potential in 2D and in 3D.

$$H = \frac{p_e^2}{2m_e^*} + \frac{1}{2}m_e^*\omega^2 r_e^2 + \frac{p_h^2}{2m_h^*} + \frac{1}{2}m_h^*\omega^2 r_h^2 - 2V_0 - \frac{e^2}{\varepsilon|r_e - r_h|} \tag{8}$$

The Hamiltonian (8) is separable in terms of the relative coordinate r and center-of-mass coordinate R defined by,

$$r = r_e - r_h \quad ; \qquad R = \left(m_e^* r_e + m_h^* r_h\right)/M \tag{9}$$

where $= m_e + m_h$. The electron and hole momenta p_e and p_h can be expressed in terms of the relative momentum $p = -i\hbar\nabla_r$ and the center-of-mass momentum $P = -i\hbar\nabla_R$ as

$$p_e = p + \left(\frac{m_e^*}{M}\right)P \; ; \quad p_e = -\,p + \left(\frac{m_h^*}{M}\right)P \tag{10}$$

Substituting (9) and (10), the Hamiltonian (8) can be written in the dimensional form as

$$H = H_R + H_r \tag{11}$$

$$H_R = -\nabla_R^2 + \frac{1}{4}\omega^2 R^2 \tag{12}$$

$$H_r = -\nabla_r^2 + \frac{1}{4}\omega^2 r^2 - \frac{2}{r} - 2V_0 \tag{13}$$

with

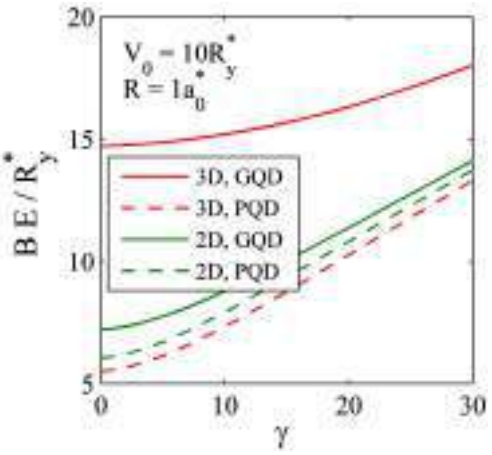

Figure 5: BE's of of an exciton in PQD and GQD as a function of the magnetic field in 2D and 3D.

$$\omega = \left[(1-\lambda)\frac{\omega_0^2}{2} + \frac{\omega_c^2}{8} + \frac{2\omega\lambda V_0}{3} - \frac{2\omega\lambda V_0}{3}\left(\frac{\omega R^2}{1+\omega R^2}\right)^{3/2} \right] \qquad (14)$$

where all energies are measured in units of the Rydberg $R_y^* = \left(\frac{\mu e^4}{2\hbar^2\varepsilon^2}\right)$, $\mu\,(=[m_e^* m_h^*]/M)$ being the reduced mass, the lengths in units of the Bhor radius $a_0^* = \left(\frac{\hbar^2\varepsilon}{\mu e^2}\right)$ and the magnetic field as $\gamma = e/2\mu c R_y^*$. If $\psi\,(r_e, r_h)$ is the eigenfunction of H , then we can write: $\psi\,(r_e, r_h) = \chi\,(R)\,\phi\,(r)$, $\chi\,(R)$ and $\phi\,(r)$ being the eigenfunctions of H_R and H_r belonging to the eigenvalues E_R and E respectively. Then exciton energy is thus given by: $E = E_R + E_r$, where $E_R = 3\omega/2$ for the GS in a three-dimensional (3D)system. The exact analytical evaluation of E_r is not possible in general. So we use the Ritz variational method and choose the trial function as: $\phi\,(r) = Ne^{-\alpha r^2 - \beta r}$, where α and β are variational parameters and N is the normalization constant. The variational energy is given by: $E_r = \langle \phi\,(r)\,|H_R|\phi\,(r)\rangle$. The exciton binding energy (BE) E_b is defined as: $E_b = (E_e + E_h - E)$, where E_e and E_h are respectively the electron and hole GS energies in the same QD.

Results and Discussion

We calculate the GS energy and BE of an exciton in a GaAs QD placed in an external magnetic field. For the material parameters we choose: $\varepsilon = 12.5$

, $m_e^* = 0.067m_e$ and $m_h^* = 0.09m_e$ (light-hole mass) and thus we have $a_0^* = 98.7A^\circ$, $R_y^* = 5.83meV$ and $1\gamma = 0.148B\,(T)$

In Fig. 1 we have shown the variation of the exciton GS energy of a light-hole exciton in a 3D GaAs QD as a function of QD effective size (R) for three values of V_0 and for both parabolic and Gaussian confinement. As the size of the QD decreases, the exciton energy monotonically increases and this increase becomes very rapid below a certain critical value of the QD size. As the depth of the confinement potential increases, the exciton energy becomes lower and lower. The decrease is essentially linear as shown in Fig. 2. The Gaussian confinement model gives a lower energy as compared to a parabolic model.

Fig. 3 shows the variation of the exciton BE as function of the QD size. It is evident that BE increases as the dot size reduces. This is understandable because with a decrease in the dot size, the spatial overlap between an electron and a hole increases leading to a stronger coulomb binding. In 3D, the binding is much stronger for Gaussian confinement than the parabolic one, particularly for small dots, whereas in 2D the binding is slightly larger for a GQD, that too at a small dot size. For a GQD, BE is larger in 3D than in 2D, whereas for a PQD, BE is slightly larger in 2D than in 3D. When the dot size becomes rather large, the dimensionality, the size and the detailed nature of the confining potential have no significant effect on the ecxiton binding.

In Fig 4 we show the variation of the exciton BE as a function of the potential depth V_0 . In general, BE increases with V_0. In 3D GQD, the rate of increase is quite significant and it is nonlinear. Again we see that exciton BE in a 3D GQD is much larger than that in a 2D GQD. But in the case of a PQD, BE is larger in 2D than in 3D. In Fig. 5 we plot the behavior of the exciton BE as a function of the magnetic field. As expected, BE increases with increasing γ . Again we see that BE is much larger in 3D GQD than in 3D PQD and 2D GQD.

Conclusion

In the present paper, we have calculated the GS energy and binding energy in a GQD in two and three dimensions in the presence of an external magnetic field using the Ritz variational method. We have also compared our results with those for the corresponding parabolic model. We have shown that the exciton energy decreases with increasing potential depth and increases with decreasing QD size and becomes significantly large below a certain critical size. We have furthermore shown that the exciton binding energy increases with decreasing dot size and in 3D, it is underestimated by the parabolic potential model as compared to that by the Gaussian model. In a 3D GQD, we have found that the binding increases as the potential becomes deeper.

The binding is also found to be enhanced by the magnetic field.

References

[1] Ka-Di Zhu and Shi-Wei Gu, *Physics Letters A*, **171**, 113, (1992).

[2] P. Bhattacharya, et al., *IEEE Trans Electron Devices*, **46,** 871 (1999).

[3] A. Kastner, *Rev. Mod. Phys.*, **64,** 849 (1992).

[4] D. Gammon, E. S. Snow, B. V. Shanabrook, D. S. Katzer and D. Park, *Phy. Rev. Lett*, **76,** 3005 (1996).

[5] J. Gu, J.Liang, *Phy. Lett. A*, **323,** 132 (2004).

[6] R.D Schaller and V.I Klimov, *Phys. Rev.Lett*, **92** 186601(2004).

[7] A.Khan, K.Balakrishnan and T.Katona, *Nat. Photonics*, **2** 77 (2008).

[8] G. T Einevoll, *Phy. Rev. B*, **45,** 3410 (1992).

[9] T. Takagahara and K. Takeda, *Phy. Rev. B*, **46,** 15578(1992).

[10] C. Sikorski and U. Merkt, *Phys. Rev. Lett.*, **62**, 2164 (1989).

[11] M. Meurer, D. Heitmann, K. Ploog, *Phys. Rev. Lett.*, **68,** 1371(1992).

[12] F. M. Peeters, *Phys. Rev. B*, **42**, 1486 (1990).

[13] S. K. Yip, *Phys. Rev. B*, **43**, 1707 (1991).

[14] S. Mukhopadhyay and A. Chatterjee, *Phys. Lett. A*, **204**, 411 (1995).

[15] S. Mukhopadhyay and A. Chatterjee, *Phys. Rev. B*, **55**, 9297 (1997).

[16] S. Mukhopadhyay and A. Chatterjee, *Phys. Rev. B*, **58**, 2088 (1998).

[17] S. Mukhopadhyay and A. Chatterjee, *Phys. Lett. A*, **240**, 100 (1998).

[18] S. Mukhopadhyay and A. Chatterjee, *Phys. Lett. A*, **242**, 355 (1998).

[19] S. Mukhopadhyay and A. Chatterjee, *Phys. Rev. B*, **59**R, 7833 (1999).

[20] S. Mukhopadhyay and A. Chatterjee, *J. Phys.: Condens. Matter*, **11**, 2071 (1999).

[21] S. Mukhopdhyay and A. Chatterjee, *Acta Phys. Pol. B*, **32**, 473 (2001).

[22] Z. Xia, *J. Appl. Phy*, **86,** 4509 (1999).

[23] W. Xie, Physics B **358,** 109 (2005).

[24] W. Que, Phys. Rev. B **45** 11036 (1992).

[25] V. Halonen, T. Chakraborty and P. Pietiläinen, *Phys.Rev.B*, **45,** 5980 (1992).

[26] S.Jaziri and R.Bennaceur, *Semicond.Sci.Technol.*, **9**, 1775(1994).

[27] J. Adamowski, M. Sobkowicz, B. Szafran, and S. Bednarek, *Phys. Rev. B*, **62,** 4234 (2000).

[28] J. Gu and J. Q. Liang, *Physics Letters A*, **335**, 451(2005).

[29] W. F. Xie, *Chin. Phys. Lett.*, **23**, 193(2006).

[30] B. Boyacioglu, M. Saglam, and A. Chatterjee, *J. Phys.: Condens. Matter*, **19**, 456217(2007).

[31] W. Xie, *Physica B*, **403**, 2828 (2008).

[32] Y. P. Bao and W.F. Xie, *Commun. Theor. Phys.*, **50**, 1449(2008).

[33] J. H. Yuan, J. S. Huan, M. Yin, Q. J. Zeng and J. P. Zhang, *Commun. Theor. Phys.* (Beijing, China), **54,** 369 (2010).

[34] S. S. Gomez, R. H. Romero, *Physica E*, **42,** 1563 (2010)

[35] G.Gharaati and R. Khordad, *Superlattices and Microstruct.* **48**, 276 (2010).

[36] A. Boda and A. Chatterjee, Physica E **45,** 36 (2012)

[37] B. Boyacioglu and A. Chatterjee, Physica B **407,** 3535(2012).

[38] B. Boyacioglu and A. Chatterjee, *J. Appl. Phys.*, **112**, 083514 (2012)

[39] A. Boda B. Boyacioglu and A. Chatterjee, *J. Appl. Phys.*, **114**, 044311 (2013).

[40] A. Boda and A Chatterjee, *Superlattices and Microstruct.*, **71**,261 (2014).

[41] A. Boda and A. Chatterjee, *Physica B*, **448,** 244 (2014)

[42] A. Boda, M. Gorre and A. Chatterjee, *Superlattices and Microstruct.*, **71,** 261 (2014).

[43] A. Boda and A. Chatterjee, *Physica B*, **448**, 244 (2014).

[44] B. Boyacioglu and A. Chatterjee, *J. Appl. Phys.*, **112,** 083514 (2012)

[45] B. Boyacioglu and A. Chatterjee, *Physica B*, **407,** 3535(2012).

[46] K. L. Jahan,I. V. Sankar, A. Boda, C. N. Raju and A.Chatterjee, *Scientific reports*, **8**, 5073 (2018).

A study of alpha and cluster radioactivity from Plutonium isotopes

Nithu Ashok
Department of Physics, S.A.R.B.T.M Government College,Koyilandy,
Kozhikode, Kerala-673305

Abstract

The probable alpha and cluster decay modes in Plutonium isotopes have been investigated with the aid of Effective Liquid Drop Model(ELDM). The predicted half-lives are compared with Universal Decay Law(UDL) and Scaling Law of Horoi et al. Geiger-Nutall plots for alpha and cluster decays are studied and are found to be linear. It is also observed that the cluster emission slows down with the increase of neutron number.

Introduction

The spontaneous emission of a fragment heavier than alpha particle and lighter than the lightest fission fragment is known as cluster radioactivity. The group of nucleons emitted as a single entity from a nucleus is called a cluster. The process of cluster radioactivity was first predicted theoretically by Sandulescu et al in 1980 [1]. Later in 1984, Rose and Jones experimentally confirmed it. They detected the emission of ^{14}C from ^{223}Ra isotope[2]. Cluster radioactivity is one of the cold nuclear phenomenon[3] predicted based on Quantum Mechanical Fragmentation Theory(QMFT)[4]. Cluster radioactivity is an intermediate process between alpha decay and spontaneous fission[5].The probability of formation of a cluster is mainly determined by its binding energy. This implies that of all the possible clusters, the alpha particle cluster is most prominent. Cluster radioactivity can be studied using two different theoretical models: Preformed Cluster Model(PCM) and Unified Fission Model(UFM). In PCM, the cluster is assumed to be preformed inside the parent nucleus. The preformation probability has to be calculated explicitly. In UFM, parent nucleus undergo continuous dynamical changes through a molecular phase until it become two separate nuclei ie. daughter and the emitted cluster. Here the preformation probability is taken as unity. The present study is carried out using UFM. The penetrability factor is calculated using Effective Liquid Drop Model(ELDM). In

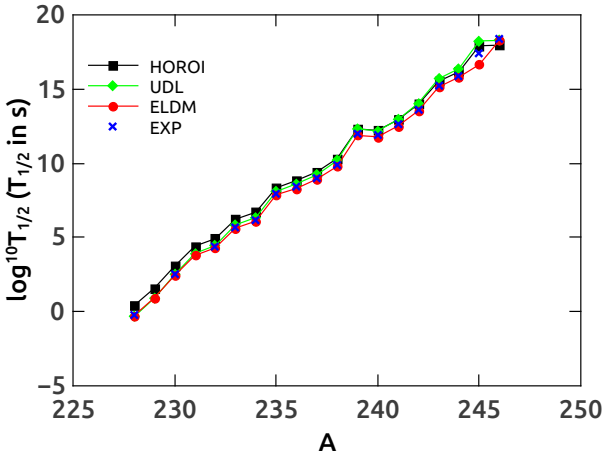

Figure 1: $\alpha-$decay half-lives of Pu isotopes as a function of mass number of parent nuclei.

this study we made an attempt to estimate the feasibility of alpha decay and cluster radioactivity in proton rich Plutonium (Pu) isotopes. Here we have looked for decays with half lives less than 10^{30}s. We have studied the isotopes in the mass range between 162 and 190. We have found out the half lives of alpha decay and cluster emission from Pu isotopes. The estimated values for alpha decay and cluster emission from Pu isotopes were compared with those evaluated based on the Universal Decay Law(UDL) and Scaling law of Horoi et al.

Theoretical Model

We have chosen the Effective Liquid Drop Model(ELDM), in which alpha decay and cluster radioactivity are explained in a unified framework. These processes are explained by taking into account different inertial coefficient according to the shape parametrization chosen to explain dynamical evolution of the system. To study the shape parametrization, four independent co-ordinates are selected[5]. In the present case, this multidimensional problem is reduced to one dimensional by imposing certain constraints.

In this model, we consider only Coulomb and surface potential energy contribution to the deformation energy of the system. The Coulomb potential which was developed by Gaudin[6] is given by

$$V_c = \frac{8}{9}\pi a^5 \epsilon(x_1, x_2)\rho_c \tag{1}$$

The surface potential is obtained by

$$V_s = \sigma_{eff}(S_1 + S_2) \tag{2}$$

where σ_{eff} is the effective surface tension.
The effect of centrifugal potential is not included in the molecular phase. It is considered only after the scission point. It is given by

$$V_l = (\hbar^2/2\mu)l(l+1)/\zeta^2 \tag{3}$$

Thus total potential in one dimensional case is given by

$$V = V_c + V_s + V_l \tag{4}$$

The barrier penetrability factor P is calculated using one-dimensional WKB approximation.

$$P = exp\{-\frac{2}{\hbar}\int_{\zeta_o}^{\zeta_c}\sqrt{2\mu(V-Q)}d\zeta\} \tag{5}$$

The limits of integration corresponds to inner and outer turning points. Q is the Q-value of the reaction ie. difference between the energies of initial and final configuration of the system or the energy released in the disintegration process. Q-value is calculated using mass excess taken from AME 2012[9]. The inertia coefficient μ is determined using Werner-Wheeler inertia coefficient[8]. The decay constant is calculated as

$$\lambda = \nu_o P \tag{6}$$

where ν_o is the assault frequency and it is approximately equal to $10^{22}s^{-1}$ for even A and $10^{-20}s^{-1}$ for odd A parent nuclei[7]. Finally half life for the decay is obtained as

$$T_{1/2} = \frac{ln2}{\lambda} \tag{7}$$

To Check the correctness of our model we have also calculated half lives using two well established formulae. One is the Universal Decay Law(UDL) which has been deduced from WKB approximation with some modifications[10]. Logarithmic form of UDL is given by

$$log_{10}T_{1/2} = aZ_cZ_d\sqrt{\frac{A}{Q_c}} + b\sqrt{AZ_cZ_d(A^{\frac{1}{3}} + A^{\frac{1}{3}})} + c \tag{8}$$

where the constants are $a = 0.4314$, $b = 0.4087$ and $c = 25.7725$.

Second one is the Scaling law proposed by Horoi et al[11]. It is given by

$$log_{10}T_{1/2} = (a_1\sqrt{\mu} + b_1)\left(\frac{(Z_cZ_d)^y}{\sqrt{Q}} - 7\right) + a_2\sqrt{\mu} + b_2 \tag{9}$$

where the constants are $a_1 = 9.1$, $b_1 = -10.2$, $a_2 = 7.39$, $b_2 = -23.2$, $x = 0.416$ and $y = 0.613$ and $\mu = \frac{A_c A_d}{A_c + A_d}$.

Both these laws are well applicable for alpha decay as well as cluster radioactivity.

Results and Discussion

Here we did a systematic study of the feasibility of α and cluster radioactivity of Plutonium isotopes ranging from A = 228 to 246 with the help of Effective Liquid Drop Model. We have considered the possible $\alpha-$ like decay modes of Plutonium isotopes within the measurable range ($T_{1/2} < 10^{30} s$).

Initially, our aim is to predict the feasibility of alpha decay from Pu isotopes as it is the most favourable decay mode. It is observed that the isotopes ranging from A=228 to 246 are unstable against alpha decay. The results have been compared with the available experimental values[12]. We have also compared our results with two well established semi-empirical laws(UDL and Scaling law of Horoi et al.). Fig. 1 shows the half-lives of alpha decay as a function of mass number of parent nuclei. From the figure, we can observe that our predicted half-lives are in good agreement with the available experimental values and also with the semi-empirical formulae.

In the second part of the study, we extended our study to analyse the possible cluster decay modes in Pu isotopes which falls in the measurable range. We have predicted the various modes of decay like ^{8}Be, ^{12}C, ^{16}O, ^{20}Ne and ^{24}Mg. The predicted half-lives are given in table 1. The calculated result shows that isotopes in the mass range A=228 to 232 are unstable against ^{8}Be decay. Similarly, mass range suitable for ^{12}C decay are A=228-234, for ^{16}O decay are A=228-233, for ^{20}Ne decay are A=228-232 and for ^{24}Mg decay are A=228-233. In addition to that, we also observed that the most probable decay corresponds to that, which leads to a magic daughter nuclei (N=126) or in its vicinity. This affirms the role of magicity in cluster radioactivity. It can also be seen that, the probility of cluster emission decreases with increase of neutron number. This shows that these decay modes are more favourable in the neutron deficient region. In fig.2, we have shown the Geiger-Nuttall plot for α and cluster emissions. From the figure, we can observe that all the decay modes shows linear behaviour. Corresponding slopes and intercepts are given in the table 2. It is found that as the cluster emitted becomes heavier, the slope increases. In general we can arrive at the formula,

$$log_{10} T_{1/2} = \frac{X}{\sqrt{Q}} + Y \tag{10}$$

which reproduces Geiger Nuttal law.

Table 1: Logarithmic half-lives of alpha and cluster emission from Pu isotopes

A	Mode of decay	$log_{10}T_{1/2}$		
		ELDM	UDL	Horoi
228		17.615	19.447	17.282
229		20.633	22.670	20.373
230	^{8}Be	23.099	25.285	22.888
231		26.196	28.455	25.930
232		28.321	30.781	28.171
233		31.029	33.610	30.889
228		15.45	17.165	14.124
229		17.871	19.842	16.579
230		20.317	22.530	19.0455
231	^{12}C	23.328	25.755	21.994
232		25.148	27.779	23.863
233		27.575	30.407	26.275
234		30.296	33.329	28.952
228		15.385	16.540	13.778
229		17.802	19.275	16.165
230		20.668	22.491	18.964
231	^{16}O	23.672	25.794	21.836
232		26.042	28.460	24.166
233		29.275	32.023	27.260
234		31.775	34.765	29.654
228		22.993	24.348	21.141
229		22.623	23.943	20.880
230	^{20}Ne	23.827	25.315	22.060
231		27.074	28.926	25.059
232		30.229	32.493	28.022
228		24.522	25.222	23.082
229		24.480	25.187	23.132
230	^{24}Mg	24.988	25.781	23.669
231		24.885	25.636	23.633
232		25.652	26.549	24.419
233		29.00	30.345	27.449
234		32.766	34.586	30.825

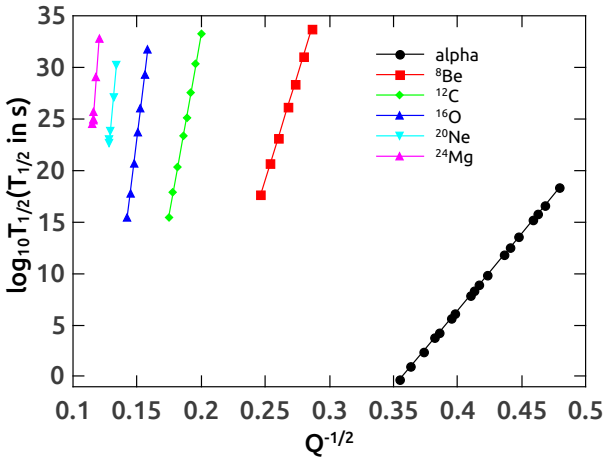

Figure 2: Geiger-Nuttall plots for various decay modes.

Table 2: Slopes and intercept values of Gieger-Nuttall plots for different clusters emitted from Pu isotopes.

Cluster	Slope X	Intercept Y
^{4}He	149.04	-50.007
^{8}Be	405.32	-82.25
^{12}C	697.36	-106.37
^{16}O	1011.45	-128.44
^{20}Ne	1341.02	-149.34
^{24}Mg	1663.26	-167.50

Conclusion

Within the framework of Effective liquid drop model, we have carried out a systematic study of the feasibility of α and cluster decay in Plutonium isotopes. Predicted $\alpha-$decay half-lives are in good agreement with the available experimental values. We also observed the decay modes like ^{8}Be, ^{12}C, ^{16}O, ^{20}Ne and ^{24}Mg in Pu isotopes. A comparitive study using the two semi-empirical formulae, UDL and Scaling Law of Horoi et al., have also been done and it is found that they agree with each other over a wide range. We have also observed that as the neutron number of the parent nuclei increases, the rate of α and cluster decay decreases, which shows these phenomena dominates in the neutron deficient region. We have also plotted GN plot which reproduces the linear nature of the graph. The study can act as a helping guide for the experimentalist in future.

References

[1] A Sandulescu, D N Poenaru and W Greiner, *Fiz. Elem. Chastits At. Yadra II*, 1334 (1980) [Sov. J. Part. Nucl. II, 528 (1980)] .

[2] H J Rose and G A Jones, *Nature (London)*, **307**, 245 (1984).

[3] R K Gupta, *Pramana-J. Phys.*, 53,3(1999).

[4] R K Gupta, in *H*eavy elements and related new phenomena edited by R K Gupta and W Greiner *World Scientific Publication, Singapore*, 1999 vol. 1, p. 536

[5] S. B. Duarte, O. A. P. Tavares, F. Guzman and A. Dimarco, *Atomic data and Nuclear data tables* , **80** , (2002), 235.

[6] M. Gaudin, *J. Phys. (France) ,* **35** *, (1974), 885.*

[7] Y.J. Shi and W.J. Swiatecki, *Nucl. Phy. A*, **464**, 205(1987).

[8] M. Goncalves and S. B. Duarte, *Phys. Rev. , C*, **48**, 2409(1993),.

[9] M.Wang, G.Audi, A.H.Wapstra, F.G.Kondev,M.MacCormick, X.Xu, and B.Pfeiffer, *CPC*, 2012, 36(12): 1603-2014.

[10] Dongdong Ni, Zhongzhou Ren, Tiekuang Dong, and Chang Xu, *Phys. Rev., C*, **78**, (2008), 044310.

[11] M.Horoi, *J.* Phys. G: Nucl. Part. Phys., **30**, 945(2004).

[12] S. B. Duarte, O. A. P. Tavares, F. Guzman and A. Dimarco, *At. Data and Nucl. Data Table*, **80**, 235(2002), V. Yu. Denisov, A. A. Khudenko, *At. Data and Nucl. Data Table*, **95**, 815(2009).